1992

Using size sensitivities to guide structural shape optimization

Afshin Mikaili
Iowa State University

INFORMATION TO USERS

This manuscript has been reproduced from the microfilm master. UMI films the text directly from the original or copy submitted. Thus, some thesis and dissertation copies are in typewriter face, while others may be from any type of computer printer.

The quality of this reproduction is dependent upon the quality of the copy submitted. Broken or indistinct print, colored or poor quality illustrations and photographs, print bleedthrough, substandard margins, and improper alignment can adversely affect reproduction.

In the unlikely event that the author did not send UMI a complete manuscript and there are missing pages, these will be noted. Also, if unauthorized copyright material had to be removed, a note will indicate the deletion.

Oversize materials (e.g., maps, drawings, charts) are reproduced by sectioning the original, beginning at the upper left-hand corner and continuing from left to right in equal sections with small overlaps. Each original is also photographed in one exposure and is included in reduced form at the back of the book.

Photographs included in the original manuscript have been reproduced xerographically in this copy. Higher quality 6" x 9" black and white photographic prints are available for any photographs or illustrations appearing in this copy for an additional charge. Contact UMI directly to order.

U·M·I

University Microfilms International
A Bell & Howell Information Company
300 North Zeeb Road, Ann Arbor, MI 48106-1346 USA
313/761-4700 800/521-0600

Order Number 9311515

Using size sensitivities to guide structural shape optimization

Mikaili, Afshin, Ph.D.

Iowa State University, 1992

U·M·I

300 N. Zeeb Rd.
Ann Arbor, MI 48106

Using size sensitivities to guide

structural shape optimization

by

Afshin Mikaili

A Dissertation Submitted to the

Graduate Faculty in Partial Fulfillment of the

Requirements for the Degree of

DOCTOR OF PHILOSOPHY

Department: Mechanical Engineering
Major: Mechanical Engineering

Approved:

Signature was redacted for privacy.

In Charge of Major Work

Signature was redacted for privacy.

For the Major Department

Signature was redacted for privacy.

For the Graduate College

Iowa State University
Ames, Iowa
1992

TABLE OF CONTENTS

LIST OF TABLES

LIST OF FIGURES

ACKNOWLEDGMENTS

I would like to thank my major professor James Bernard for his friendship and guidance over the past few years. I would also like to thank professors Hindman, Pierson, Rogge, and Vanderploeg for taking part in my committee and for providing their valuable advice.

A special thanks to my friends and colleagues, Jeff Trom, Jay Shannan, Jim Lynch, Todd Teske, Jim Troy, Terran Boylan, Dave Shrader, Allen Li, and Judy Vance for their technical assistance and for the welcomed diversions they helped provide.

Finally, I would like to thank my family: Mostafa, Hajar, Arman, Ramin, Linda, and the little guy Boris for their love, support, and inspiration.

1. INTRODUCTION

Finite–element–based structural optimization has two main areas of focus. The first is size optimization, where cross–sectional dimensions of a finite element (e.g., thickness of a plate element) or a grouping of finite elements are varied to improve the response of the structure. The second is shape optimization, where the overall dimensions of a finite element (e.g., width and length of a plate element) or a grouping of finite elements are subject to change. Figure 1.1 illustrates this distinction.

Shape optimization presents two challenges. The first derives from the need for a continuously changing finite element topology. Automated mesh generation has been addressed as an integral component of shape redesign [1] and optimum mesh refinement has been shown to be closely coupled with the development of an optimum shape [2].

The second challenge presented by shape optimization is the need for the calculation of grid sensitivities, that is, the need to place quantitative measures on how the structural response varies as the coordinates of a grid point or a grouping of grid points are varied. Grid sensitivities are calculated either by differentiation of the finite element model, or by differentiation of the continuum equations. The former method has proven to be computationally expensive, while the latter method leads to numerical difficulties due to the need for the calculation of boundary integrals.

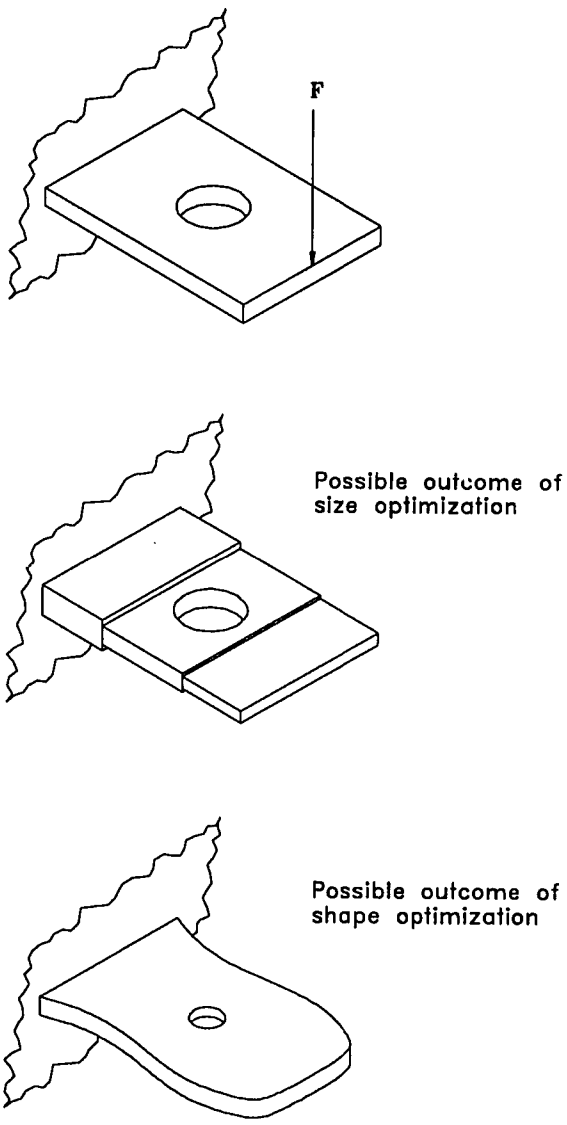

Figure 1.1: Size and shape optimization

The use of domain integrals instead of boundary integrals to alleviate the numerical difficulties results in calculations which are nearly as expensive as the former method [3].

This thesis presents an alternate method for shape redesign based on Nearly Zero Section (NZS) elements. Ref. [4] introduced these elements in the form of flange, web, and latch–type reinforcements as a tool for selecting the most effective reinforcement configurations. In the method presented here, the free surfaces of the finite element model of a structure are coated with NZS elements. Because of their small thickness, the incorporation of these elements does not significantly affect the structural performance. The sensitivities of the structural response with respect to the thickness of the NZS elements provide qualitative insight into the behavior of the structure as well as a quantitative basis for optimization.

In the pre–processing stage, the NZS method requires the creation of a thin layer of shell elements over the chosen free surfaces of the finite element model. This is shown schematically by Figure 1.2. Finite element pre–processors (see, for example, Ref. [5]) typically provide efficient means of creating shell elements on the free faces of user–selected solid elements.

The method can also be applied when the underlying structure consists of plate elements. As Figure 1.3 shows, NZS beam elements are used to line selected free edges – in the case shown, the free edges of an opening at the center of a plate structure. These elements use the existing nodes of the plate elements and are therefore of the same length as the underlying plate elements. They are also specified to have the same width as the plate elements, while the thickness; i.e., the dimension normal to the free edge, is assigned a nearly zero value.

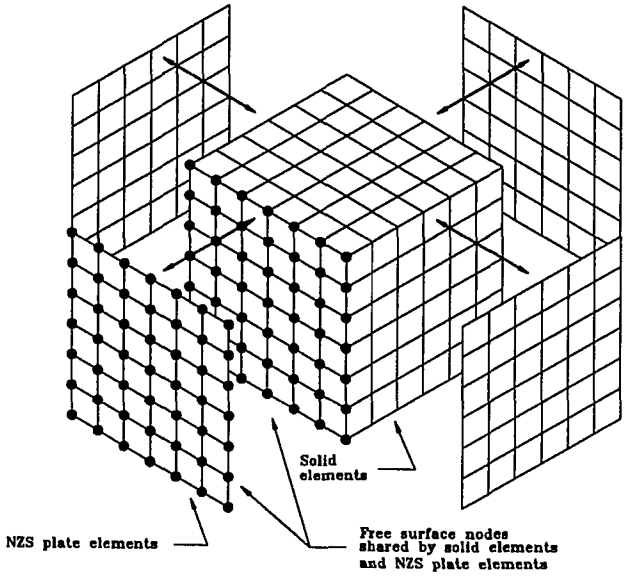

Figure 1.2: NZS shell elements coating the free faces of solid elements

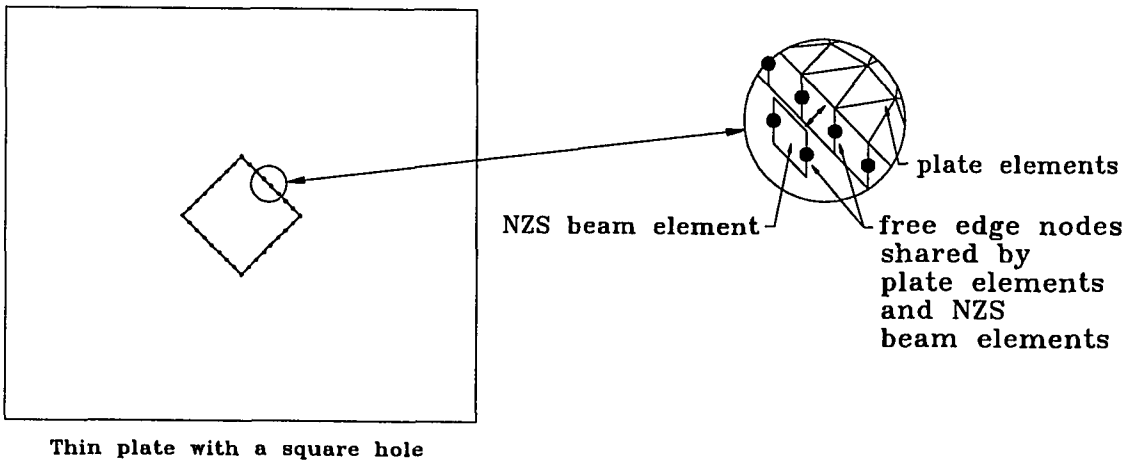

Figure 1.3: NZS beam elements lining the free edges of plate elements

Once the pre–processing stage is complete, Finite Element Analysis (FEA), and Design Sensitivity Analysis (DSA) yield the desired response of the structure and the sensitivity of the response with respect to the thickness of each NZS element. In the work presented in this thesis, structured solution sequences 101 and 103 of MSC/NASTRAN [6] were used for static and normal mode analyses, respectively.

As will be demonstrated in the case studies, post–processing of the sensitivities in the form of contour plots provides valuable insight on the behavior of the structure. The sensitivities are also an integral part of the shape redesign methods which will be introduced.

The following chapter will give formulation of three different approaches to the problem of shape redesign using NZS sensitivities. In the first approach, it is assumed that there are no imposed geometric constraints. In this "free–field" approach, the sensitivities are used directly to modify the location of the surface nodes with no geometric constraints on the movement of the nodes. The second approach concerns the case where only changes in dimensional parameters of the structure (e.g., a shaft diameter, or a fillet radius) are allowed. An algorithm is introduced to calculate these "parameter–based" sensitivities from the NZS sensitivities. The third approach considers the class of structural optimization problems where the shape is free to change in any fashion, but there are imposed constraints on some geometric property such as weight. A method for incorporating the NZS sensitivities and these "property–based" geometric constraints in a constrained minimization formulation is introduced.

Subsequent chapters give applications for each of the three methods. In Chapter 3 the free–field approach is used to change the shape of a cantilever beam, modeled with solid elements, with the goal of reducing its end–displacement under transverse

gravitational loading. Another application involving the fundamental frequency of a thin plate is also given in this chapter to illustrate how the method can be used on structures modeled with plate elements.

In Chapter 4 the maximum principal stress in a pin geometry under static loading is considered. As in the free–field method, the sensitivities of the response variable with respect to the thickness of each NZS element are first computed. However, rather than using these sensitivities directly to alter the geometry of the pin, the NZS sensitivities are used to predict changes in the stress as a result of proposed changes in the stem radius and/or fillet radius of the pin, and to compute parameter–based sensitivities.

Chapter 5 considers the inverse elasticity problem of minimizing the stress concentration around an opening in a thin plate under biaxial loading. With some simplifying assumptions, researchers have analytically found the optimality condition to be a uniform tangential stress along the boundary of the opening (see, for example, Ref. [7, 8, 9, 10, 11]). In Chapter 5 this optimization problem is solved computationally under a property–based geometric constraint of constant opening area. Chapter 6 presents conclusions.

2. SHAPE REDESIGN USING NEARLY ZERO SECTION SENSITIVITIES

The shape redesign method presented in this thesis is based on creating a Nearly Zero Section (NZS) coating of elements on the free surfaces of an existing finite element model of a structure, and calculating the sensitivity of the response variables with respect to the thickness of each of the NZS elements. The NZS sensitivities are then used in one of three different ways:

1. Free–field redesign
2. Redesign subject to parameter–based geometric constraints
3. Redesign subject to property–based geometric constraints

In free–field redesign, it is assumed that there are no imposed geometric constraints. NZS sensitivities are used directly to modify the location of the surface nodes with no imposed geometric constraints on the movement of the nodes.

For a large class of structural problems, however, there is an implicit constraint (imposed by manufacturing, aesthetic, or other considerations) of keeping the general shape characteristics of the structure intact. For this class of problems, only changes in the dimensional parameters of the structure (e.g., a shaft diameter, or a fillet radius) are allowed. For these problems, NZS sensitivities are calculated in the same

manner as in the free–field method, but are not directly used to modify the shape of the structure. Instead, they are used to build a linear prediction model for the response of the structure, and to calculate desired parameter–based sensitivities.

There are also cases where the shape of the structure is free to change in any fashion, but there are imposed constraints on properties such as weight. These property–based geometric constraints are incorporated in a constrained minimization formulation. The minimization is based on a linear model which is constructed using the NZS sensitivities.

2.1 Free–field Redesign

Once NZS sensitivities are computed, they can be directly used to modify the location of free surface nodes. Figure 2.1 shows a two dimensional representation of the problem. $\underline{V}_1$ and $\underline{V}_2$ are vectors whose directions are normal to the elements surrounding a given node i and whose magnitudes are proportional to the calculated sensitivities. The sense of these vectors depends on the desired sense of change in the magnitude of the response variable. For example, if a natural frequency is the response variable and it is desired to increase this frequency, positive sensitivities suggest addition of material while negative sensitivities suggest removal of material. Figure 2.1 corresponds to such a scenario with an assumed positive sensitivity for the element to the left of node i and a negative sensitivity for the element to the right of node i.

The heavy solid lines in Figure 2.1 indicate the new boundary of the structure if the edges of the underlying solid elements are moved in the direction normal to the NZS elements. Although this would be the literal interpretation of the trends

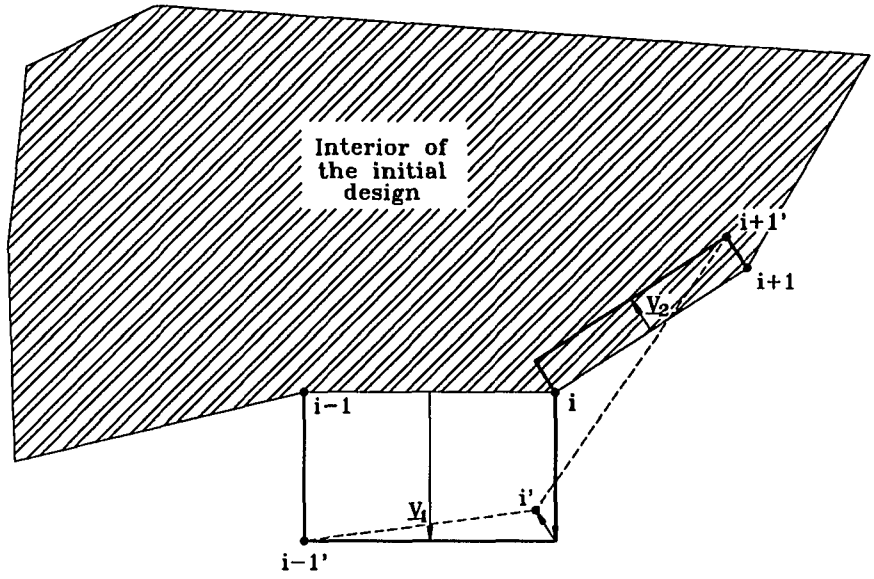

Figure 2.1: Movement of free surface nodes (2D)

suggested by the sensitivities, it would lead to difficulties in the remeshing process. In Figure 2.1, for example, the number of nodes would increase from 3 to 7, and the roughness of the resulting boundary would most likely be unacceptable. A better alternative is to move node i by the resultant of the vectors $\underline{V}_1$ and $\underline{V}_2$. The dotted lines in Figure 2.1 show this approximation. The number of nodes remains unchanged, and the smoothness of the resulting boundary is comparable to that of the original boundary.

Therefore, the grid movement vector for node i, $\underline{\Delta}_i$, is given by:

$$\underline{\Delta}_i = \underline{V}_1 + \underline{V}_2 \tag{2.1}$$

$$\underline{\Delta}_i = d_r \frac{s_1}{s_{max}} \hat{\underline{n}}_1 + d_r \frac{s_2}{s_{max}} \hat{\underline{n}}_2 \tag{2.2}$$

where d_r is a user–specified representative distance, s_1 and s_2 are calculated sensitivities for the NZS elements surrounding node i, s_{max} is the largest sensitivity

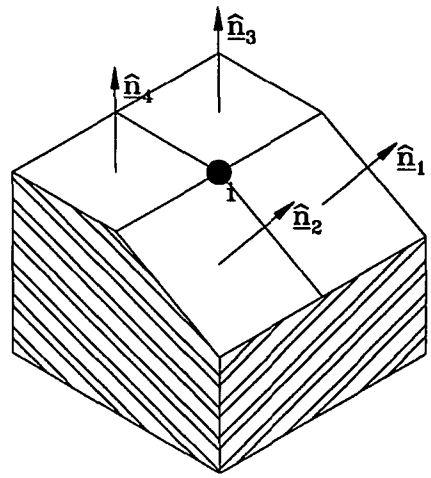

Figure 2.2: Free surface node surrounded by four NZS elements

magnitude (i.e., $max(|s_1|, |s_2|, |s_3|, \ldots)$), and $\hat{n}_1$ and $\hat{n}_2$ are unit vectors normal to the elements surrounding node i.

The extension of this procedure to three dimensions (see Figure 2.2) gives:

$$\underline{\Delta}_i = d_r \frac{1}{s_{max}} \sum_{j=1}^{J_i} s_j \hat{n}_j \tag{2.3}$$

where J_i is the number of NZS elements surrounding node i.

Use of Equation 2.3 suggests the need for some modifications. First of all, consider the intuitively based desire to preserve angles at nodes surrounded by equal sensitivities. For example, this case arises in the cantilever beam problem considered in the next chapter. As Figure 3.4 of Chapter 3 shows, equal sensitivities occur on all four sides of the beam at the free end. Therefore, shape modification should collapse the walls equally in all directions at this end of the beam.

As Figure 2.3 shows, it is clear that a right angle is preserved if the change called for by Equation 2.3 is multiplied by two. In general, it can be shown that the required magnification factor, M_{α_i}, to preserve a given angle, α_i, at a node surrounded

by equal sensitivities is given by:

$$M_{\alpha_i} = \frac{2}{1 - sin(3\pi/2 - \alpha_i)} \tag{2.4}$$

Note that if α_i is equal to zero, the magnification factor is 1.0.

Furthermore, in a general three dimensional case, a node may be shared by several NZS elements with arbitrary orientations. The question arises as to which relative angle is to be preserved. Experience leads to the decision to preserve the maximum relative angle. Thus, for a given node,i, α_i is derived from:

$$\begin{aligned} \alpha_i &= max(cos^{-1}(\underline{\hat{n}}_j \cdot \underline{\hat{n}}_k)) \\ j &= (1, \ldots, J_i) \\ k &= (1, \ldots, J_i) \\ j &\neq k \end{aligned} \tag{2.5}$$

where node i is surrounded by elements $1, \ldots, J_i$. Therefore, α_i is the maximum angle which exists between any two vectors normal to the elements surrounding node i.

Incorporation of M_{α_i} into Equation 2.3 leads to:

$$\underline{\Delta}_i = M_{\alpha_i} d_r \frac{1}{s_{max}} \sum_{j=1}^{J_i} s_j \underline{\hat{n}}_j \tag{2.6}$$

Another recurring challenge is that different surface nodes may be surrounded by different numbers of NZS elements. In the beam of Figure 3.2 of Chapter 3, for example, the nodes at the fixed and free ends are shared by only two elements, whereas the other surface nodes are shared by four elements. The summation of Equation 2.3 should, therefore, include a term to weigh grid movement vectors based on the number of elements which surround a given node.

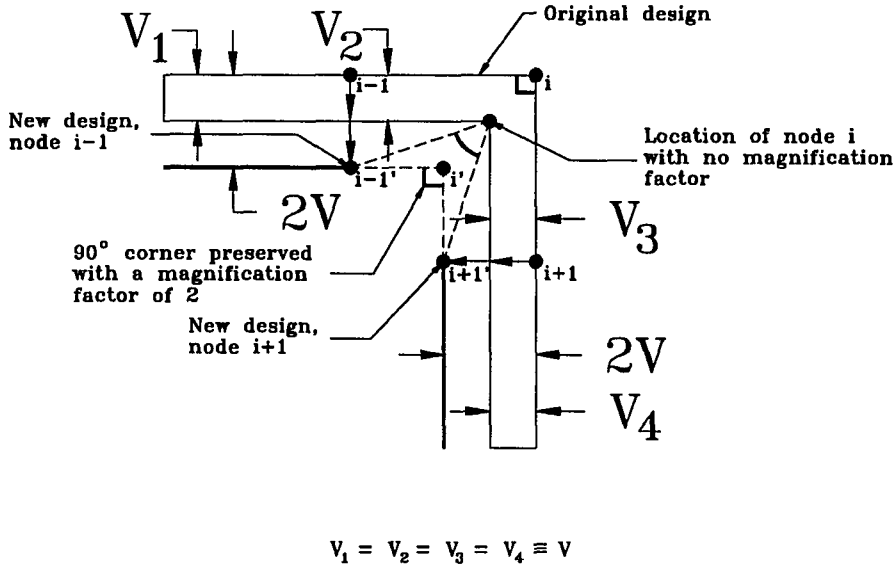

Figure 2.3: Angle dependent magnification factor for a 90° corner

A suitable weighting factor is $\frac{J_{max}}{J_i}$, where J_{max} is the maximum number of NZS elements surrounding any surface node, and J_i is the number of NZS elements surrounding node i. For the beam of Figure 3.2, $\frac{J_{max}}{J_i}$ is unity for all surface nodes except those at the fixed and free ends where it is two.

Incorporating this weighting factor and the angle dependent magnification factor, M_{α_i}, in Equation 2.3 gives:

$$\underline{\Delta}_i = \frac{J_{max}}{J_i} M_{\alpha_i} d_r \frac{1}{s_{max}} \sum_{j=1}^{J_i} s_j \underline{\hat{n}}_j \tag{2.7}$$

In essence, for the beam of Figure 3.2, the $\frac{J_{max}}{J_i}$ weighting factor applies a zero order extrapolation of the sensitivity data at the ends of the beam. This is evident by observing that in Equation 2.7, applying a $\frac{J_{max}}{J_i}$ factor of two for the end nodes is equivalent to assuming that there is a set of elements extending beyond the fixed end of the beam, and a corresponding set of elements which extends beyond the free end

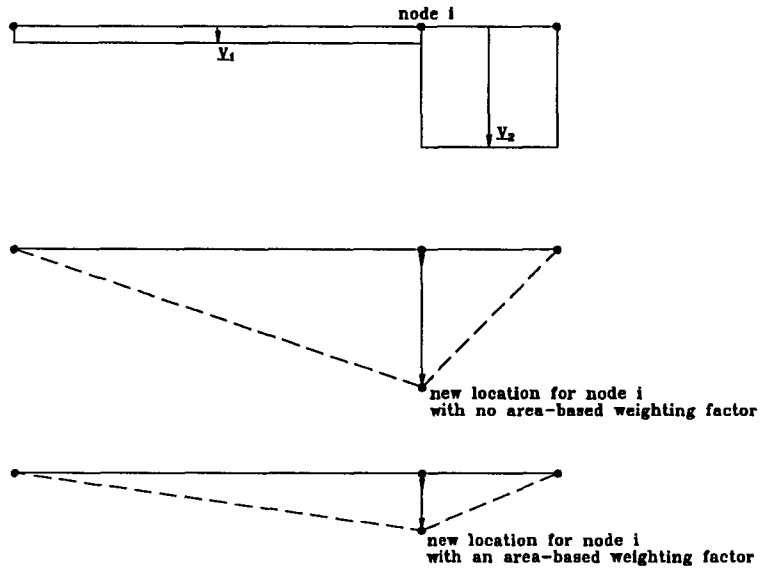

Figure 2.4: Effect of an area–based weighting factor (2D)

of the beam, and that the sensitivities for these elements are assumed to be equal to the calculated sensitivities for the elements at the corresponding ends of the beam.

A final additional term is introduced in order to account for varying areas spanned by elements. An area–based weighting factor is used to weigh the components of the grid movement vector based on the area spanned by individual elements. Figure 2.4 shows the effect of this weighting factor for a two dimensional case.

Therefore, Equation 2.7 becomes:

$$\underline{\Delta}_i = \frac{1}{A_{max_i}} \frac{J_{max}}{J_i} M_{\alpha_i} d_r \frac{1}{s_{max}} \sum_{j=1}^{J_i} A_j s_j \underline{\hat{n}}_j \tag{2.8}$$

where A_j is the area of the jth NZS element surrounding node i and A_{max_i} is the local maximum area; i.e., $max(A_1, A_2, \ldots, A_{J_i})$.

It should be noted that Equation 2.8 can be represented by:

$$\underline{\Delta}_i = f(geom) d_r \frac{1}{s_{max}} \sum_{j=1}^{J_i} s_j \underline{\hat{n}}_j \tag{2.9}$$

with $f(geom)$ being a closed form, algebraic, geometry dependent function which always yields a positive value.

2.2 Redesign Subject to Parameter–based Geometric Constraints

Oftentimes, due to manufacturing, aesthetic, or other considerations, structural shape optimization is limited to keeping the general shape characteristics of the structure unchanged. These constraints lead to the fact that only changes in the dimensional parameters of the structure (e.g., a shaft diameter, or a fillet radius) are allowed. Therefore, there is a need to translate the free–field NZS sensitivity information to parameter–based sensitivities.

Figure 2.5 shows a two dimensional cross section of a stepped shaft and the relocation of the surface nodes as the diameter of one section is changed from d_1 to d_2. Note that the mesh density is the same for the initial and modified designs. For example, there is an equal number of elements resolving the fillet region for both designs.

This criterion on the mesh makes it important to have access to an automated, parameter–based finite element pre–processor. There are many such programs available commercially. (See, for example, Ref. [5].)

It should also be noted that the mesh for the modified design is not necessarily used for finite element analysis. As will become apparent, this mesh is only needed for the geometric calculations required for computing parameter–based sensitivities.

As Figure 2.5 shows, the centroid of each (kth) NZS element undergoes a displacement of $\underline{V}_{\Delta cg_k}$. An effective thickness, V_k, can be calculated by projecting $\underline{V}_{\Delta cg_k}$

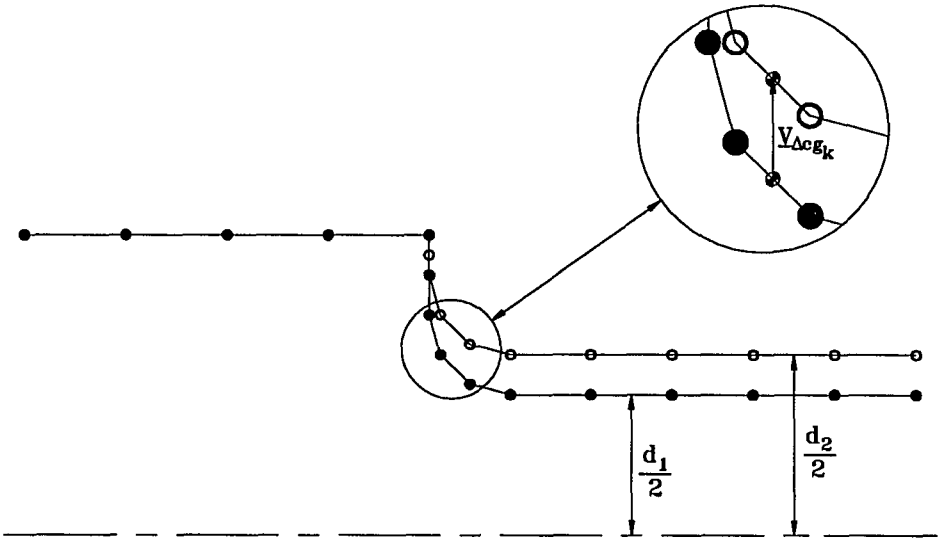

Figure 2.5: Relocation of shaft surface nodes with a change in shaft diameter (2D profile)

on the unit vector normal to the element in its initial configuration:

$$V_k = \underline{V}_{\Delta cg_k} \cdot \hat{\underline{n}}_k \tag{2.10}$$

Figure 2.6 gives a graphical representation of this equation. With the normal vector defined to point outward, a positive value from Equation 2.10 corresponds to addition of material while a negative value suggests removal of material.

The effective thicknesses, V_k, can then be used in a first order Taylor series expansion to calculate a predicted response for the lth response variable, R_l:

$$R_l = R_{l_o} + \sum_{k=1}^{N_k} \frac{\partial R_l}{\partial v_k} V_k \tag{2.11}$$

where R_{l_o} is the original response, and $\frac{\partial R_l}{\partial v_k}$ is the sensitivity of the lth response variable with respect to the kth NZS thickness.

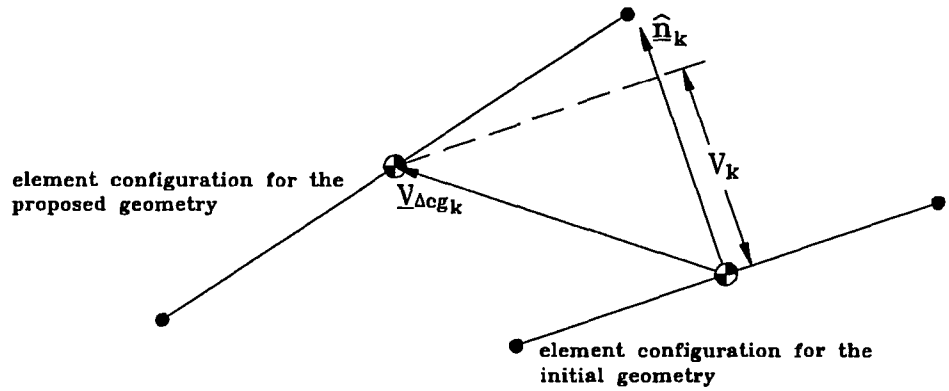

Figure 2.6: Effective material addition (2D)

Parameter–based sensitivities can, in turn, be calculated using:

$$\frac{\partial R_l}{\partial p_i} = \frac{R_l - R_{l_o}}{p_{i_n} - p_{i_o}} \tag{2.12}$$

with p_i representing a dimensional parameter such as a shaft diameter. Once parameter–based sensitivities are calculated, first order structural optimization techniques (see, for example, Ref. [12, 13]) can be used for optimization.

It is important to note that Equation 2.11 can be used with several simultaneous changes in dimensional parameters. For example, Figure 2.7 shows a case where both the fillet radius and the shaft diameter are changed. Equations 2.10, and 2.11 can still be used to predict the response of the structure. The p_i parameter of Equation 2.12 may be some independent variable which sets both the shaft diameter and the fillet radius.

2.3 Redesign Subject to Property–based Geometric Constraints

Another class of problems arises when there are imposed constraints on structural properties such as weight.

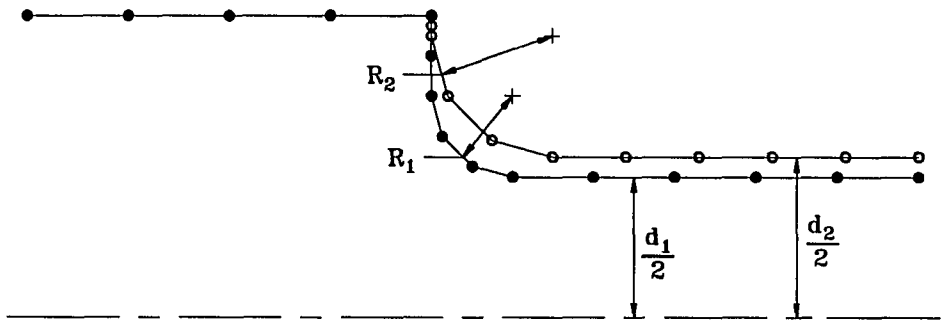

Figure 2.7: Relocation of shaft surface nodes with changes in shaft diameter and fillet radius (2D profile)

A general constrained minimization formulation could be given as:

$$\begin{aligned} &minimize\ f(R_l, \underline{\Delta}_i) \\ &subject\ to\ g(R_l, \underline{\Delta}_i) = 0 \\ &h(R_l, \underline{\Delta}_i) \leq 0 \end{aligned} \tag{2.13}$$

where the scalar merit function, f, the vector of equality constraint functions, g, and the vector of inequality constraint functions, h, are expressed in terms of the linear approximations of the response variables, R_l, and the grid locations, $\underline{\Delta}_i$.

In turn, R_l and $\underline{\Delta}_i$ are functions of the NZS thicknesses, v_k, via Equation 2.11 and a slight variation of Equation 2.9, respectively:

$$R_l = R_{l_o} + \sum_{k=1}^{N_k} \frac{\partial R_l}{\partial v_k} v_k \tag{2.14}$$

$$\underline{\Delta}_i = f(geom) d_r \frac{1}{v_{max}} \sum_{j=1}^{J_i} v_j \underline{\hat{n}}_j \tag{2.15}$$

where as before, R_{l_o} is the original response, and $\frac{\partial R_l}{\partial v_k}$ is the sensitivity of the lth response variable with respect to the kth NZS thickness. However, the grid movement equation is now based on NZS thicknesses rather than NZS sensitivities. That is, v_j

is the thickness of the jth NZS element surrounding node i, and v_{max} is the maximum thickness magnitude (i.e., $max(|v_1|, |v_2|, |v_3|, \ldots, |v_{N_k}|)$). The representative distance, d_r, which was specified by the user in the free–field approach is now set equal to the average of the magnitude of the thicknesses:

$$d_r = \frac{1}{N_k} \sum_{k=1}^{N_k} |v_k| \tag{2.16}$$

Therefore, Equations 2.13 can be more aptly expressed as:

$$\begin{aligned} &minimize\ f(R_l, \underline{\Delta}_i)_{v_k} \\ &subject\ to\ g(R_l, \underline{\Delta}_i)_{v_k} = 0 \\ &h(R_l, \underline{\Delta}_i)_{v_k} \leq 0 \end{aligned} \tag{2.17}$$

to show the dependence on the NZS thicknesses. The optimal solution, v_k^* is the set of thicknesses which minimizes f while satisfying the set of constraints g, and h.

A subset of these problems is given by:

$$\begin{aligned} &minimize\ f(R_l)_{v_k} \\ &subject\ to\ g(\underline{\Delta}_i)_{v_k} = 0 \end{aligned} \tag{2.18}$$

where there are no inequality constraints, the merit function is only a function of the response variables, and the equality constraints are only functions of the grid locations.

In Chapter 5, for example, the objective is to reduce the stress concentration around the opening in a thin plate under biaxial loading; therefore, $f(R_l)$ is expressed in terms of the square of the difference between the high stresses and a nominal stress, while $g(\underline{\Delta}_i)$ is used to keep a constant opening area.

3. APPLICATIONS: FREE–FIELD REDESIGN

This chapter gives examples for the free–field approach. In the first example, the shape of a cantilever beam, modeled with solid elements, is changed in order to reduce the end–displacement under transverse gravitational loading. The second example involves the fundamental frequency of a thin plate modeled using two different representations: solid elements coated with NZS plate elements, and plate elements lined with NZS beam elements.

3.1 Cantilever Beam Under Transverse Gravitational Loading

In this case study, we will analyze the cantilever beam of Figure 3.1 under a transverse unit gravitational load. The steel beam is 20" long and originally has a constant 3" X 3" cross section. The finite element model of Figure 3.1 consists of linear solid elements with a total of 1701 nodes; 81 of which are restrained in the x, y, and z directions at the fixed end of the beam. Figure 3.2 shows the plate elements which coat the four sides of the beam. These elements are 0.05" thick.

Since the interior nodes are coupled by solid elements only, they have no rotational degrees of freedom. However, the surface nodes are shared by plate elements as well as solid elements. These nodes have rotational degrees of freedom in addition to their translational degrees of freedom.

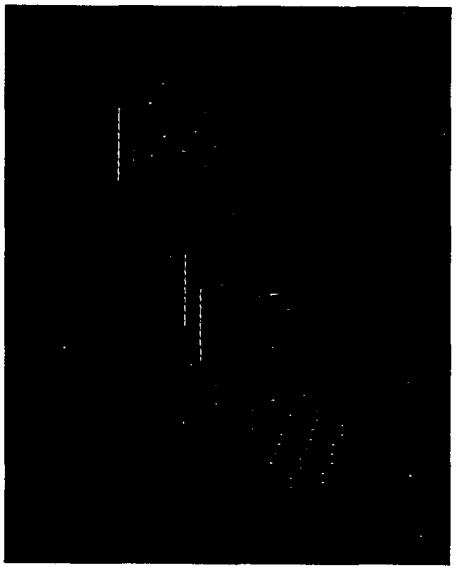

Figure 3.1: Finite element model of a 3" X 3" X 20" cantilever beam

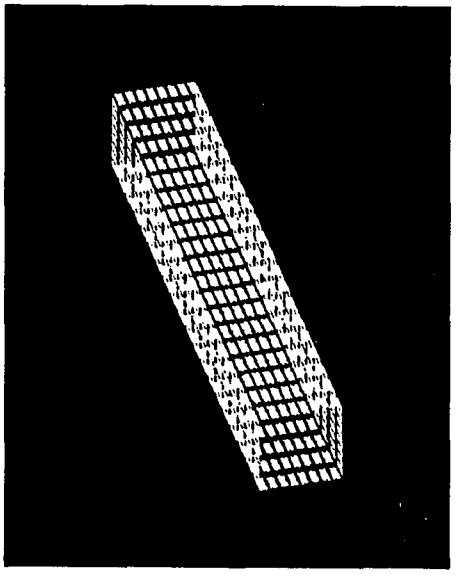

Figure 3.2: 0.05" thick NZS elements coating the sides of the beam (elements shrunk for display purposes)

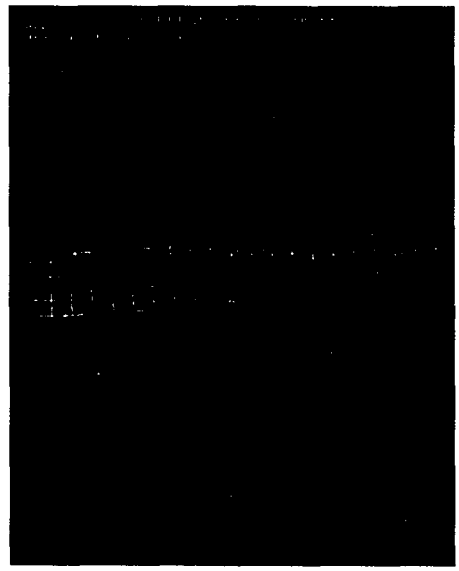

Figure 3.3: Deflected beam

FEA of the beam (including the NZS plate elements) yields the deformed shape shown in Figure 3.3. The goal is to reduce the displacement at the center of the free end of the beam, δ. Table 3.1 shows the FEA-calculated δ to be 2.37E-04". The closed form analytical solution (see, for example, Ref. [14]) yields 2.35E-04".

The table lists δ with no NZS elements to be 2.51E-04". The incorporation of

Table 3.1: End displacement of the beam

	Analytical solution	FEA solution
No NZS	2.51E-04"	2.51E-04"
NZS t=0.005"	2.49E-04"	2.50E-04"
NZS t=0.05"	2.35E-04"	2.37E-04"

NZS elements with a 0.05" thickness; therefore, introduces a 6% change in δ. The table also shows the results from a separate FEA with an NZS dimension of 0.005" to be 2.50E-04", which is very close to the 2.51E-04" with no NZS elements. Using t=0.005", however, leads to a loss of resolution (most likely due to computer round-off errors) in the calculated sensitivities. This phenomenon will be discussed shortly.

A Design Sensitivity Analysis (DSA) of the structure was conducted to calculate sensitivities of δ with respect to the thickness of the plate elements. Since the beam is symmetric, analysis was conducted only for the left half of the beam. Results were then duplicated for the right half using symmetry. (For this problem, DSA is required only for a quarter of the beam. We chose half the beam in order to verify sensitivity symmetry between the results for the upper left and lower left quarters of the beam.)

Figure 3.4 presents the results of the sensitivity analysis. The strongest positive sensitivities occur at the free end of the beam, where all four sides of the beam yield the same result. The strongest negative sensitivities are located on the upper and lower sides of the fixed end of the beam. However, at this end sensitivities reduce to zero at the neutral axis of the beam. There is a gradual transition in the sensitivities along the top and bottom surfaces from the fixed end to the free end.

The next step was to use the sensitivity results to move the free surface nodes. Using Equation 2.8, DSA results of Figure 3.4, and a representative distance, d_r, of 0.2", we obtained the beam of Figure 3.5. We arrived at the value of 0.2" for d_r by limiting the maximum $|\underline{\Delta}_i|$ for any surface node to be 1.0" and solving for the value of d_r which yields this maximum $|\underline{\Delta}_i|$. Since Equation 2.8 is linear with respect to d_r, the procedure is straightforward.

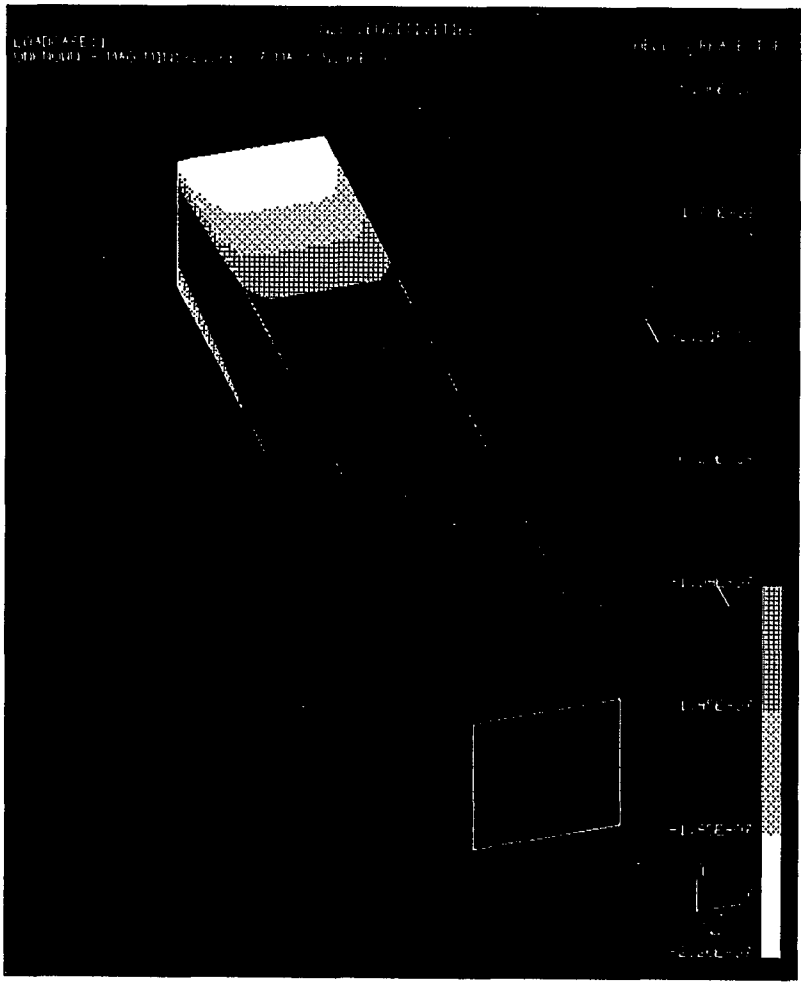

Figure 3.4: NZS sensitivities for the initial beam

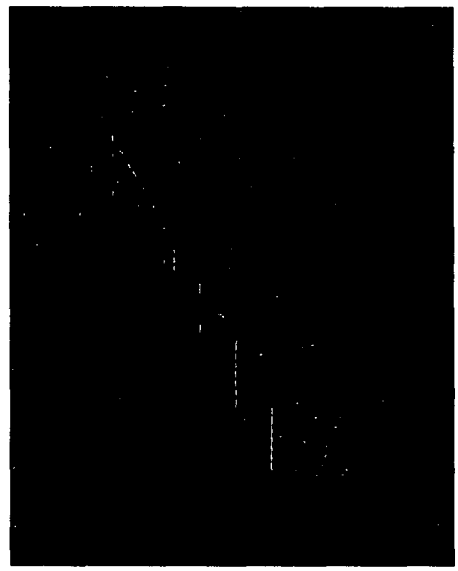

Figure 3.5: Modified cantilever beam

As Figure 3.5 shows, the beam cross section at the fixed end has grown to resemble an I–beam, whereas the walls at the free end have collapsed equally in all directions. The free end of this beam has a 2.6" X 2.6" cross section and the cross section of the fixed end has extreme points which are the vertices of a rectangle with a base of 4.2" and a height of 4.6".

In general, the mesh for the modified geometry (resulting from the application of Equation 2.8) may not be suitable for subsequent finite element analysis. For example, the aspect ratios for the outer layer of elements at the free end of the beam of Figure 3.5 are much smaller that those of the original mesh shown by Figure 3.1. Therefore, remeshing is in order.

When dealing with general three dimensional shapes, it is very important to have access to software which has the capability to manipulate the finite element mesh in a logical manner. Powerful geometrical manipulation tools are important,

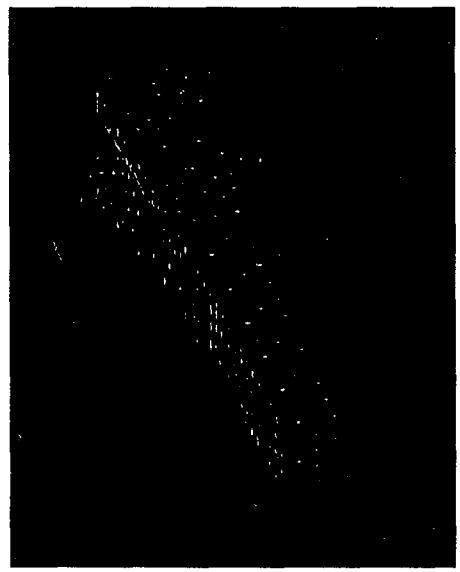

Figure 3.6: Modified cantilever beam remeshed

but relational database tools are also very important.

The I-DEAS finite element pre–processor [5] was used to remesh the beam of Figure 3.5. The software was used to detect and group the free surface nodes. Its spline fitting routines were then used to create surfaces through these nodes. An unstructured mesh consisting of linear tetrahedron elements was then cast within the closed mesh volume defined by the resulting surfaces. Figures 3.6 and 3.7 show the results.

FEA of the resulting beam (along with a new coating consisting of triangular plate elements with t=0.05") led to a δ of 8.75E-05" which is a 63% reduction from the 2.37E-04" for the beam of Figure 3.1.

In order to further reduce δ, we conducted a sensitivity analysis for the new beam with the new NZS elements. As was the case with t=0.005" for the NZS elements of Figure 3.2, sensitivities are not very well resolved using t=0.05" for the coating of

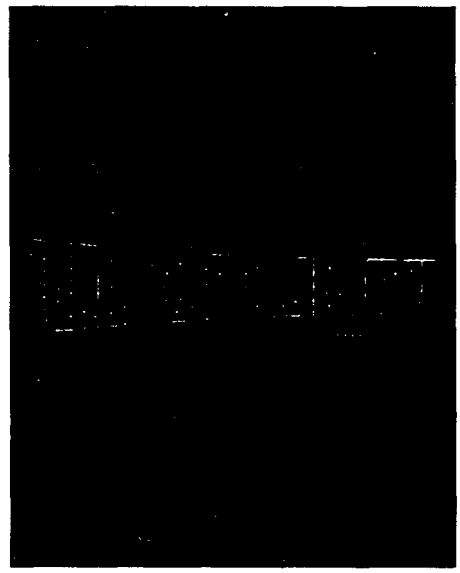

Figure 3.7: Modified cantilever beam remeshed (side view)

Figure 3.6. This phenomenon will now be investigated.

Figure 3.8 shows plots of sensitivities (sorted in ascending order) for the elements coating the beam of Figure 3.6. Three sets of sensitivities are plotted: t=0.05" Δb=0.01%, t=0.05" Δb=0.03%, and t=0.1" Δb=0.03%, where Δb is the perturbation percentage for the calculation of sensitivities (the DELTAB parameter in the MSC/NASTRAN DVAR card, [15]).

Figure 3.9 presents expanded plots from Figure 3.8. Note that there is a data point for each curve corresponding to all integer values on the abscissa. These figures show that there is a strong gradation of sensitivities with t=0.05" Δb=0.01%. The gradation is less severe with the same value of t but a larger Δb of 0.03%, and even less apparent with t=0.1" Δb=0.03%. For example, the second plot of Figure 3.9 shows that the sensitivity is calculated to be zero for a much larger number of NZS elements

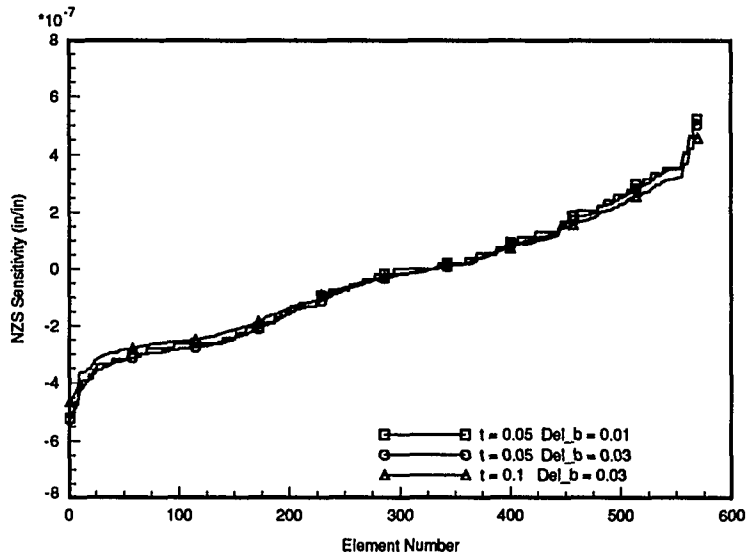

Figure 3.8: Plots of NZS sensitivities for varying t and Δb

with t=0.05" Δb=0.01%, than with t=0.05" Δb=0.03%, or t=0.1" Δb=0.03%.

Therefore, sensitivities are better resolved with larger Δb's and larger NZS thicknesses. There is a limit on how large Δb and t can be made, however, since sensitivities are less accurate as Δb is increased, and the response itself is less accurate with larger NZS thicknesses. Table 3.2 shows that δ of the beam with t=0.05" is 3% smaller than δ with no NZS elements and 5% smaller with t=0.1".

Figure 3.10 presents a contour plot of the t=0.1" Δb=0.03% sensitivities. Maximum positive sensitivities still occur at the free end while the largest negative sensitivities occur a few element lengths from the fixed end.

In order to further reduce δ, we use Equation 2.8 with the t=0.1" Δb=0.03% sensitivity results shown by Figures 3.10. Figures 3.11 and 3.12 show the resulting beam with a d_r of 0.066" (leading to a maximum $|\underline{\Delta}_i|$ of 0.5"). The free end of the beam now has a 1.9" X 1.9" cross section while the fixed end has extreme points

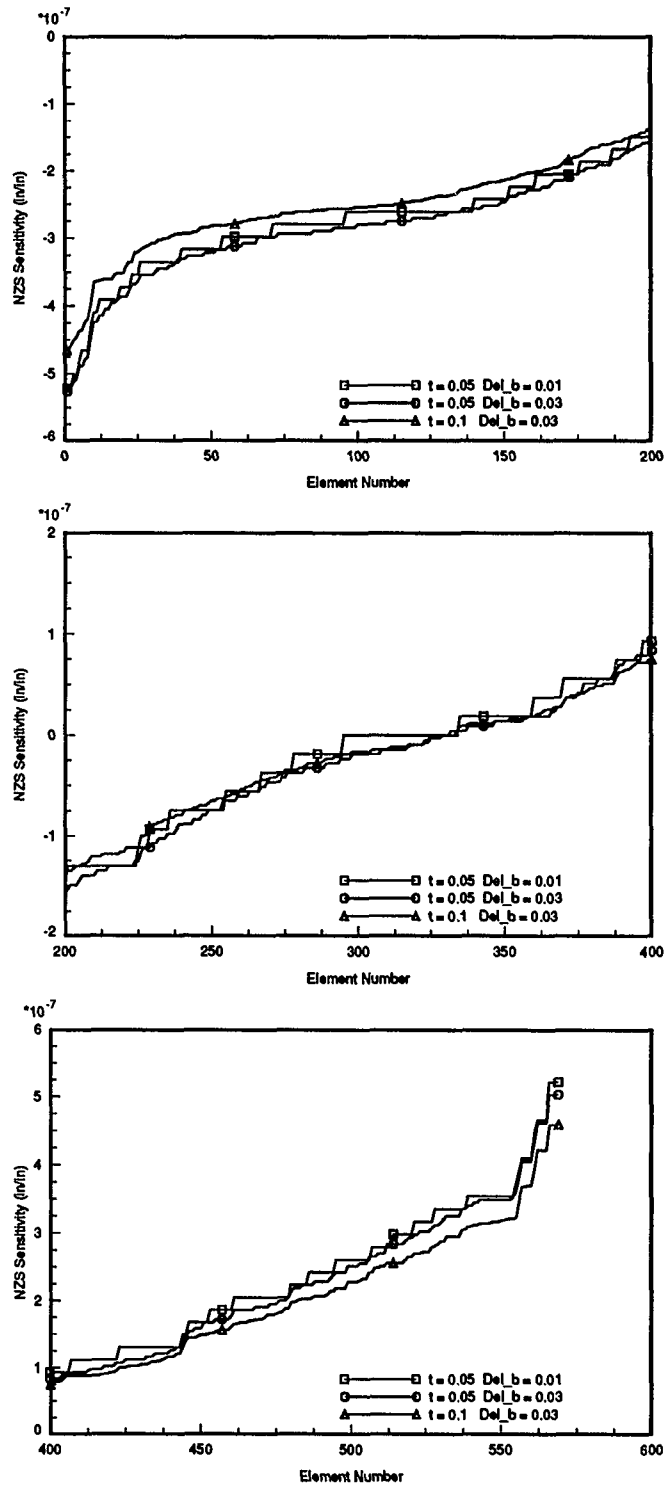

Figure 3.9: Expanded plots of NZS sensitivities for varying t and Δb

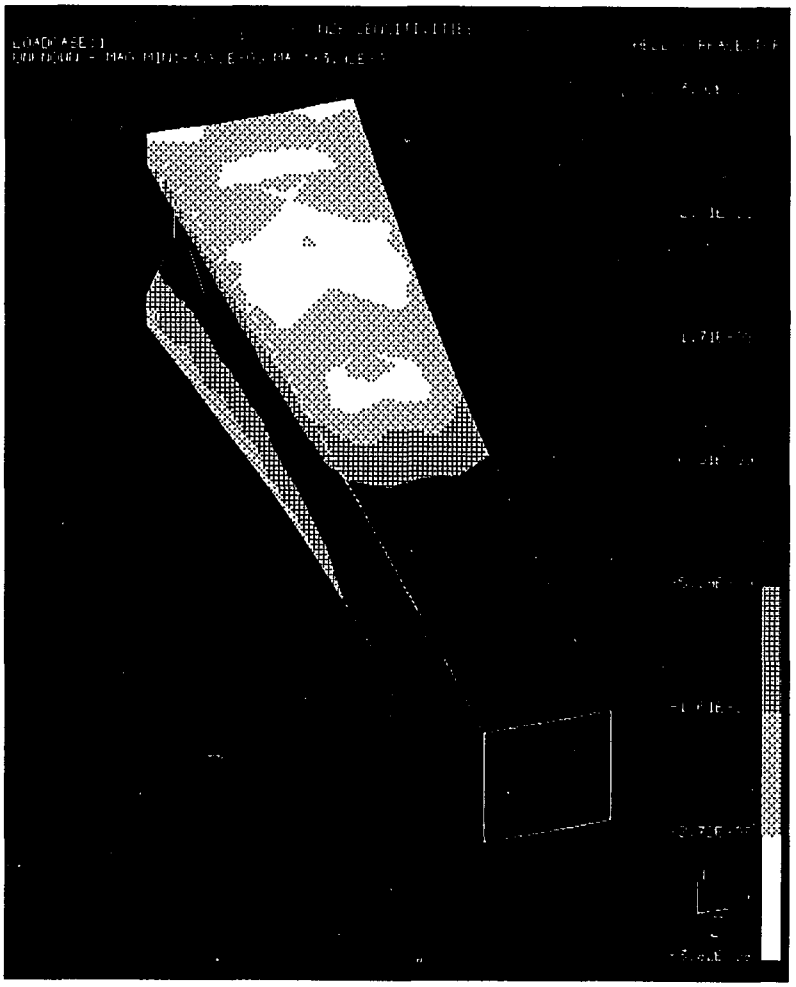

Figure 3.10: NZS sensitivities for the modified beam

Table 3.2: End displacement of the modified beam

	FEA solution
No NZS	9.02E-05"
NZS t=0.05"	8.75E-05"
NZS t=0.1"	8.51E-05"

which define the vertices of a rectangle with a base of 4.9" and a height of 5.2". FEA of this beam yielded a δ of 5.00E-05" which is a 43% reduction from 8.75E-05" for the beam of Figures 3.6 and a 79% reduction from the 2.37E-04" for the initial beam of Figures 3.1.

Table 3.3 summarizes the shape redesign of the cantilever beam. The initial FEA for the beam of Figure 3.1 with linear hexagonal elements and linear quadrilateral NZS elements required 20 minutes of CPU time on a DECstation 3100. Subsequent FEA of the redesigned beam of Figure 3.6 with linear tetrahedron elements and linear triangular NZS elements required 11 minutes. The final FEA of the beam of Figure 3.11 with linear tetrahedron elements and no NZS elements took 6 minutes. Although the latter two FEA's involve the same number of finite element nodes, the model which has NZS elements has 5030 degrees of freedom whereas the one with no NZS elements has 3372 degrees of freedom. The additional degrees of freedom are due to the rotational degrees of freedom for the surface nodes of the model with NZS elements. Corresponding DSA's took 55 minutes for the first redesign and 45 minutes for the second redesign. The two shape redesigns yielded a 79% reduction in the end-displacement of the beam.

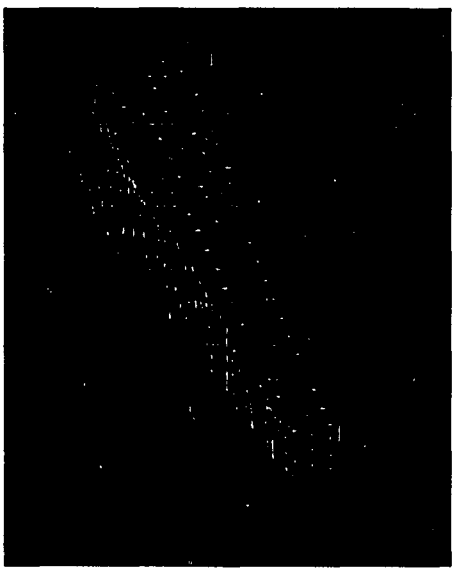

Figure 3.11: Re–modified cantilever beam

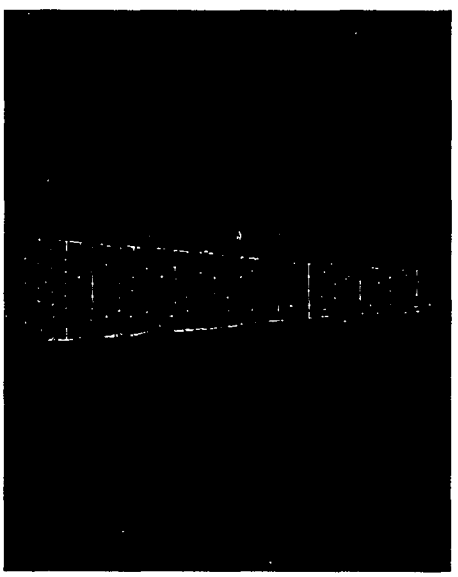

Figure 3.12: Re–modified cantilever beam (side view)

Table 3.3: Beam redesign

Design #	Number of nodes/ d.o.f.	Number of NZS sensitivities	CPU[a] FEA/ DSA (min.)	Cross section dimensions fixed/ free ends (inches)	End displacement (inches)
1	1701/ 6220	320	20/ 55	3 X 3/ 3 X 3	2.37E-04
2	1174/ 5030	569	11/ 45	4.2 X 4.6[b]/ 2.6 X 2.6	8.75E-05
3	1174/ 3372	—	6/ —	4.9 X 5.2[b]/ 1.9 X 1.9	5.00E-05

a) On a DECstation 3100.
b) Base and height dimensions of the rectangle defined by the extreme points of the I–beam cross section.

The computational cost of size–based NZS sensitivities is much lower than shape–based sensitivities. For example, an explicit finite difference method where the locations of each surface node are successively perturbed in the x, y, and z directions, FEA is conducted for each perturbation, and a forward difference is used to estimate the sensitivities would lead to CPU times which are orders of magnitude greater than those encountered in the NZS method. In the beam of Figure 3.1, for example, there are 357 surface nodes on each half of the beam. Perturbations in the x and y directions and FEA's for each perturbation (each at a cost of 20 minutes) would translate to 14280 minutes (or nearly 10 days) of CPU. Size–based NZS sensitivities led to results in 55 minutes.

3.2 Fundamental Frequency of a Thin Plate

In this section, we will analyze the fundamental frequency of a circular plate, and the sensitivity of the fundamental frequency with respect to the shape of a circular opening at the center of the plate.

Two different finite element representations are considered. We first use solid elements to model the plate and a thin coating of plate elements on the free surfaces of the solid elements surrounding the opening. This representation is very similar to the one used to analyze the cantilever beam in the previous case study. In the second representation, we use plate elements to model the structure, and a thin lining of beam elements on the free edges of the plate elements surrounding the opening.

We will also conduct similar analyses for a square plate with a circular opening at its center.

3.2.1 Circular Plate

Figure 3.13 shows the finite element model of a 20" diameter circular plate with a 6" diameter opening at its center. This model consists of linear hexagonal elements with the nodes separated by 0.15" in the z–direction (the direction perpendicular to the plate). The nodes along the outer rim of the plate are fixed in all degrees of freedom.

The first mode shape of the plate is shown by Figure 3.14. The associated natural frequency, f_m, is 168.1 Hz. The objective is to find the effect of changes in the shape of the circular opening on this frequency. The procedure is analogous to that followed for the cantilever beam problem of the previous case study.

Figures 3.15 and 3.16 show the NZS plate elements coating the free faces of the

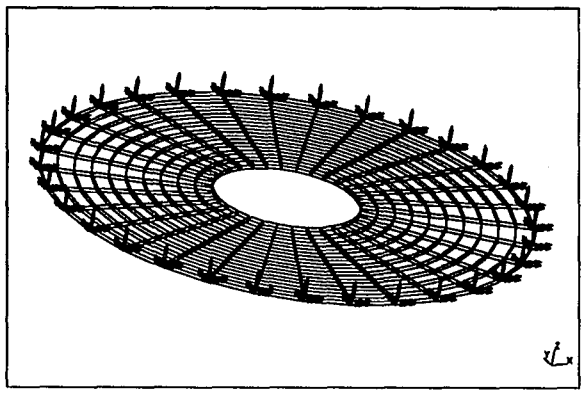

Figure 3.13: Finite element model of a circular plate (solid model)

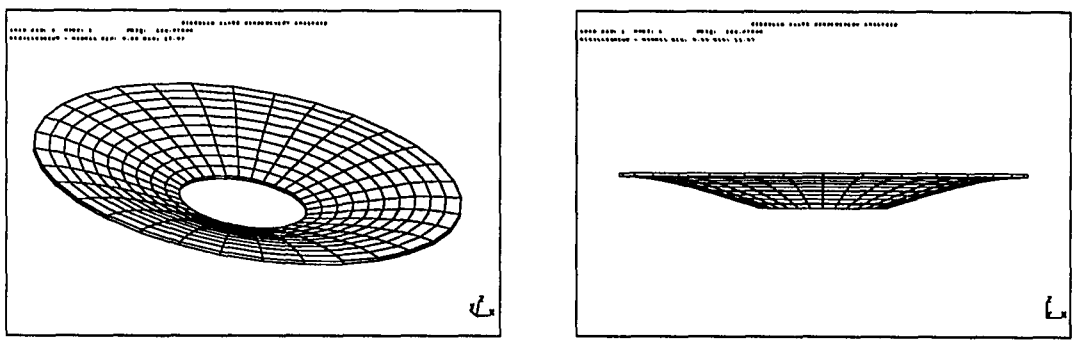

Figure 3.14: First mode of vibration, circular plate (solid model)

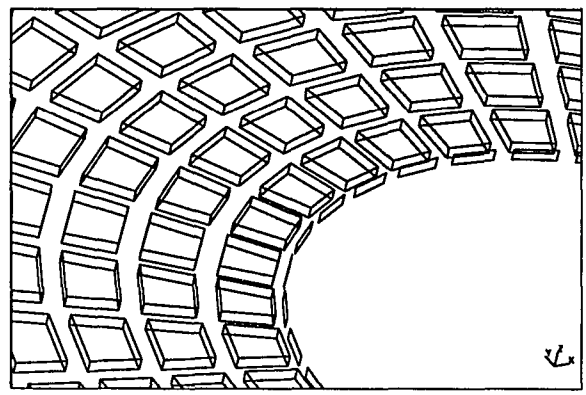

Figure 3.15: NZS plate elements, circular plate (elements shrunk for display purposes)

solid elements which surround the opening. A thickness of 0.01" is used for the NZS elements.

Table 3.4 gives the sensitivities of f_m with respect to the thickness of each plate element. As expected, for a circular plate with a circular opening, the sensitivities are essentially identical for all NZS elements. The minimum and the maximum sensitivities (-0.651 Hz/in and -0.649 Hz/in, respectively) deviate by only 0.28%. This deviation is most likely due to round–off errors.

Note that the sensitivities are negative, which implies that addition of material (i.e., reducing the size of the circular opening) will have a negative effect on f_m.

In practice, thin plates are modeled using plate elements rather than solid elements. Figure 3.17 shows such a finite element model for the circular plate. Each plate element is assigned a 0.15" thickness in the finite element formulation.

The fundamental mode shape for the plate model is shown by Figure 3.18. The corresponding natural frequency is 166.4 Hz which is in good agreement with the value of 168.1 Hz calculated for the solid model.

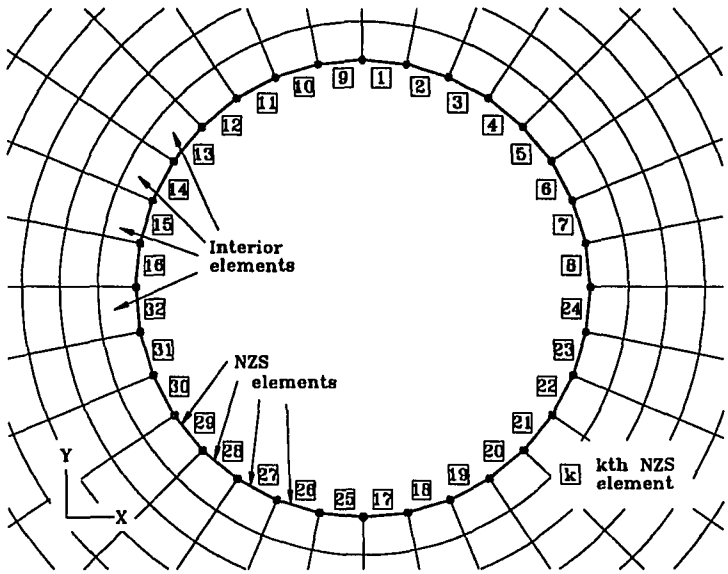

Figure 3.16: Configuration of NZS elements

Table 3.4: NZS sensitivities, circular plate (solid model) ($\frac{\partial f_m}{\partial v_k}$, Hz/in)

f_m	f_m	f_m	f_m
$v_1 : -6.4977E-01$	$v_9 : -6.4979E-01$	$v_{17} : -6.4951E-01$	$v_{25} : -6.4952E-01$
$v_2 : -6.5083E-01$	$v_{10} : -6.5093E-01$	$v_{18} : -6.5122E-01$	$v_{26} : -6.5132E-01$
$v_3 : -6.5089E-01$	$v_{11} : -6.5103E-01$	$v_{19} : -6.5102E-01$	$v_{27} : -6.5116E-01$
$v_4 : -6.5001E-01$	$v_{12} : -6.4992E-01$	$v_{20} : -6.4965E-01$	$v_{28} : -6.4956E-01$
$v_5 : -6.5001E-01$	$v_{13} : -6.4965E-01$	$v_{21} : -6.4992E-01$	$v_{29} : -6.4956E-01$
$v_6 : -6.5089E-01$	$v_{14} : -6.5102E-01$	$v_{22} : -6.5103E-01$	$v_{30} : -6.5116E-01$
$v_7 : -6.5083E-01$	$v_{15} : -6.5122E-01$	$v_{23} : -6.5093E-01$	$v_{31} : -6.5132E-01$
$v_8 : -6.4977E-01$	$v_{16} : -6.4951E-01$	$v_{24} : -6.4979E-01$	$v_{32} : -6.4952E-01$

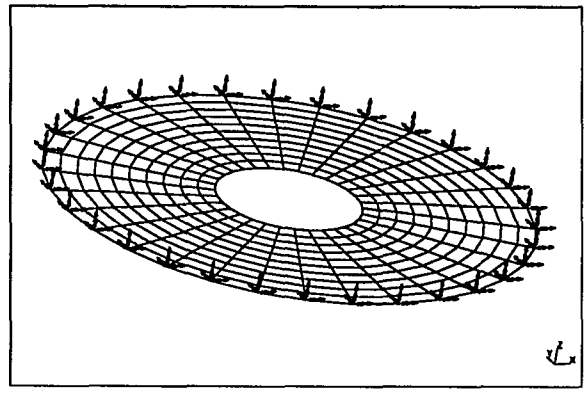

Figure 3.17: Finite element model of a circular plate (plate model)

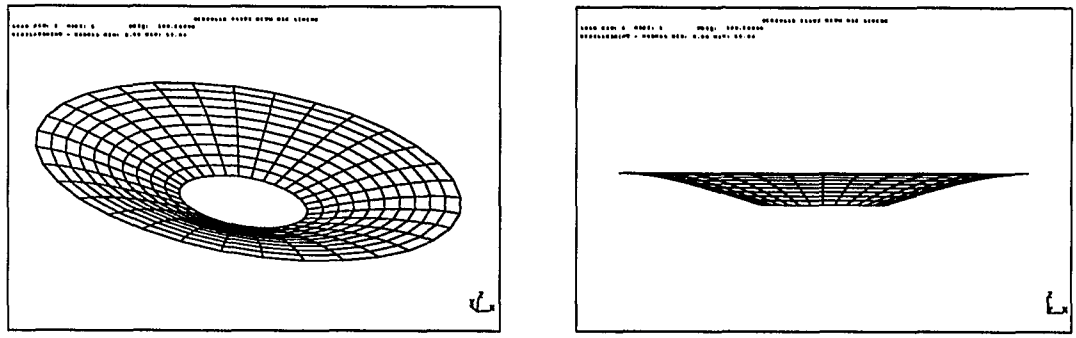

Figure 3.18: First mode of vibration, circular plate (plate model)

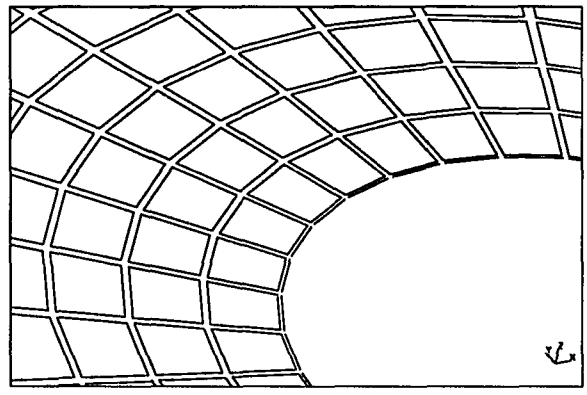

Figure 3.19: NZS beam elements, circular plate (elements shrunk for display purposes)

Figure 3.19 shows the NZS beam elements lining the free edges of the plate elements which surround the opening. These elements are assigned a 0.15" depth in the z–direction (i.e., the direction perpendicular to the plate) and a thickness of 0.01". Therefore, the dimensions of these beam elements are equal to those of the NZS plate elements shown by Figure 3.15.

Table 3.5 gives the sensitivities of f_m with respect to the thickness of each beam element. These sensitivities are very similar to those given by Table 3.4.

3.2.2 Square Plate

We now consider the plate geometry of Figure 3.20. The 20" X 20" X 0.15" plate has a 6" diameter opening at its center. The model consists of linear wedge elements with the nodes separated by 0.15" in the z–direction (the direction perpendicular to the plate). The plate is restrained in all degrees of freedom on its outer edges.

Figure 3.21 shows the first mode of vibration. The fundamental frequency, f_m, is 148.6 Hz.

Table 3.5: NZS sensitivities, circular plate (plate model) ($\frac{\partial f_m}{\partial v_k}$, Hz/in)

f_m	f_m	f_m	f_m
$v_1 : -6.8025E-01$	$v_9 : -6.8026E-01$	$v_{17} : -6.8006E-01$	$v_{25} : -6.8007E-01$
$v_2 : -6.8137E-01$	$v_{10} : -6.8155E-01$	$v_{18} : -6.8136E-01$	$v_{26} : -6.8153E-01$
$v_3 : -6.8071E-01$	$v_{11} : -6.8080E-01$	$v_{19} : -6.8143E-01$	$v_{27} : -6.8152E-01$
$v_4 : -6.8083E-01$	$v_{12} : -6.8073E-01$	$v_{20} : -6.8019E-01$	$v_{28} : -6.8009E-01$
$v_5 : -6.8083E-01$	$v_{13} : -6.8019E-01$	$v_{21} : -6.8073E-01$	$v_{29} : -6.8009E-01$
$v_6 : -6.8071E-01$	$v_{14} : -6.8143E-01$	$v_{22} : -6.8080E-01$	$v_{30} : -6.8152E-01$
$v_7 : -6.8137E-01$	$v_{15} : -6.8136E-01$	$v_{23} : -6.8155E-01$	$v_{31} : -6.8153E-01$
$v_8 : -6.8025E-01$	$v_{16} : -6.8006E-01$	$v_{24} : -6.8026E-01$	$v_{32} : -6.8007E-01$

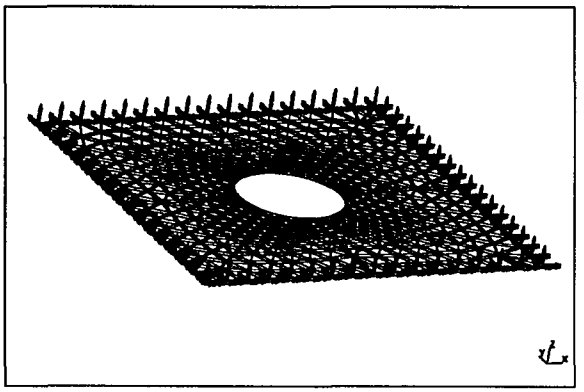

Figure 3.20: Finite element model of a square plate (solid model)

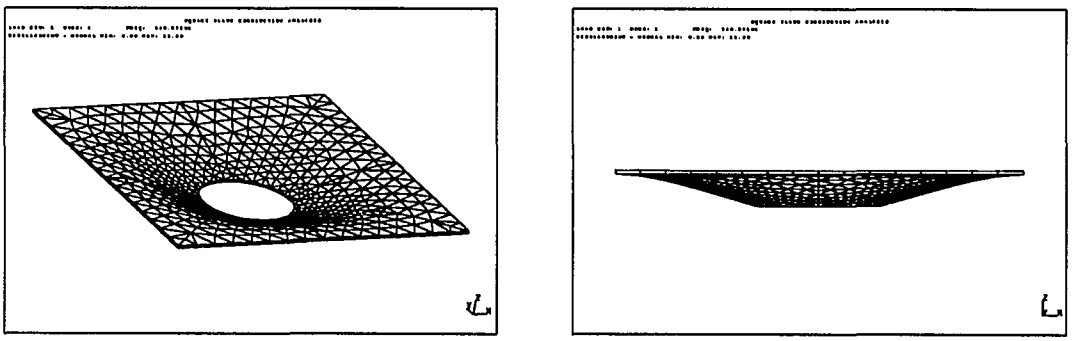

Figure 3.21: First mode of vibration, square plate (solid model)

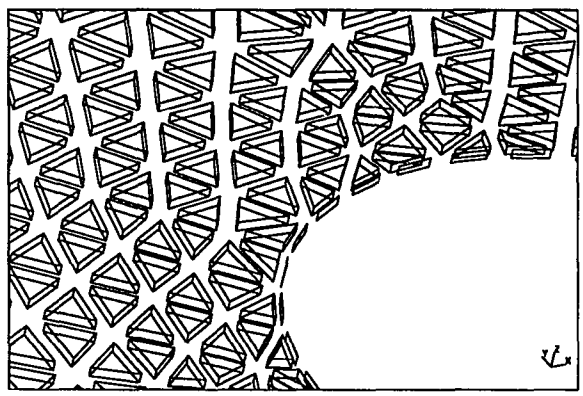

Figure 3.22: NZS plate elements, square plate (elements shrunk for display purposes)

Figure 3.22 shows the NZS plate elements coating the free faces of the wedge elements surrounding the opening. The NZS elements are assigned a thickness of 0.01". They are numbered in the same manner as in the circular plate problem (as given by Figure 3.16).

Table 3.6 presents the sensitivities of f_m with respect to the thickness of each plate element. As with the circular plate, the sensitivities are negative. Therefore, closing the opening will reduce f_m. However, for the square plate, the magnitude of the sensitivities vary along the edge of the opening. The sensitivities range from -0.462 Hz/in for elements 4, 5, 12, 13, 20, 21, 28, 29 (i.e., NZS elements closest to the diagonal axes of the square plate) to -0.521 Hz/in for elements 1, 8, 9, 16, 17, 24, 25, 32 (i.e., NZS elements closest to the vertical and horizontal axes of the square plate).

As with the circular plate, the analysis for the square plate was repeated using plate elements rather than solid elements, and NZS beam elements instead of NZS plate elements. Figures 3.23, 3.24, and 3.25 show the resulting finite element model, fundamental mode shape, and NZS beam elements, respectively. The fundamental

Table 3.6: NZS sensitivities, square plate (solid model) ($\frac{\partial f_m}{\partial v_k}$, Hz/in)

f_m	f_m	f_m	f_m
$v_1 : -5.2150E-01$	$v_9 : -5.2151E-01$	$v_{17} : -5.2135E-01$	$v_{25} : -5.2137E-01$
$v_2 : -5.0700E-01$	$v_{10} : -5.0711E-01$	$v_{18} : -5.0723E-01$	$v_{26} : -5.0734E-01$
$v_3 : -4.7700E-01$	$v_{11} : -4.7730E-01$	$v_{19} : -4.7695E-01$	$v_{27} : -4.7726E-01$
$v_4 : -4.6258E-01$	$v_{12} : -4.6225E-01$	$v_{20} : -4.6250E-01$	$v_{28} : -4.6217E-01$
$v_5 : -4.6258E-01$	$v_{13} : -4.6250E-01$	$v_{21} : -4.6225E-01$	$v_{29} : -4.6217E-01$
$v_6 : -4.7700E-01$	$v_{14} : -4.7695E-01$	$v_{22} : -4.7725E-01$	$v_{30} : -4.7721E-01$
$v_7 : -5.0700E-01$	$v_{15} : -5.0723E-01$	$v_{23} : -5.0715E-01$	$v_{31} : -5.0738E-01$
$v_8 : -5.2150E-01$	$v_{16} : -5.2135E-01$	$v_{24} : -5.2151E-01$	$v_{32} : -5.2137E-01$

frequency for this plate model is 143.4 Hz (compared to 148.6 Hz for the solid model of Figure 3.20).

Table 3.7 presents the calculated sensitivities for the NZS beam elements. These results closely match the results for the NZS plate elements given by Table 3.6.

Equation 2.8 can now be used to modify the shape of the opening with the objective of increasing f_m. For the plate of Figures 3.23, all values of $\frac{J_{max}}{J_i}$, and $\frac{A_j}{A_{max_i}}$ are equal to one, and M_{α_i} is very nearly equal to one. Also, each free edge node is shared by two NZS beam elements; i.e., $J_i = 2$. Therefore, Equation 2.8 simplifies to:

$$\underline{\Delta}_i = d_r \frac{1}{s_{max}} \sum_{j=1}^{2} s_j \hat{\underline{n}}_j \tag{3.1}$$

Using this equation, the sensitivities of Table 3.7, and a d_r value of 1.005" (yielding a maximum $|\underline{\Delta}_i|$ of 2.0") results in the new node locations shown by Figure 3.26.

Figure 3.27 shows a finite element mesh for the modified plate. Finite element analysis yielded the fundamental mode shape shown by Figure 3.28 and a correspond-

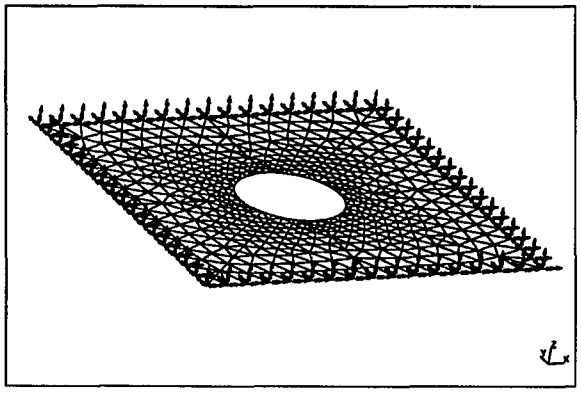

Figure 3.23: Finite element model of a square plate (plate model)

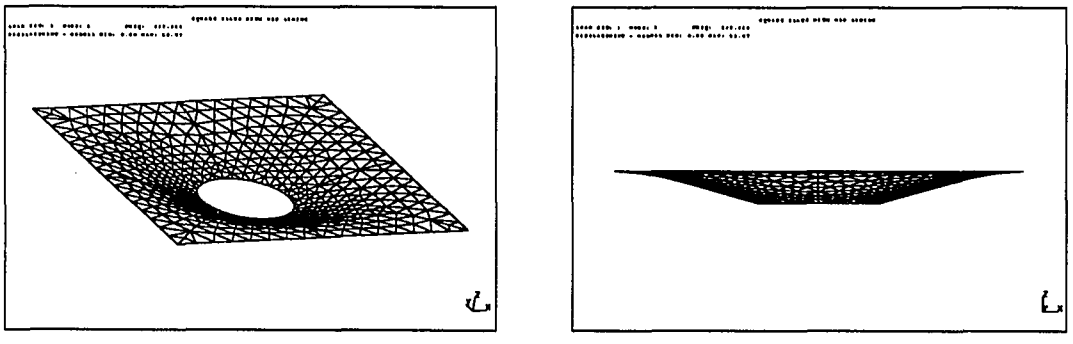

Figure 3.24: First mode of vibration, square plate (plate model)

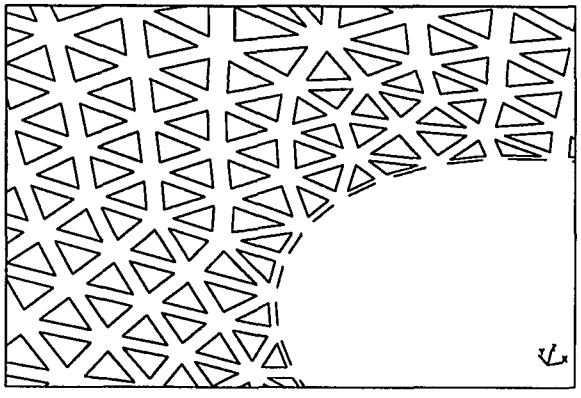

Figure 3.25: NZS beam elements, square plate (elements shrunk for display purposes)

Table 3.7: NZS sensitivities, square plate (plate model) ($\frac{\partial f_m}{\partial v_k}$, Hz/in)

f_m	f_m	f_m	f_m
$v_1 : -5.1292E-01$	$v_9 : -5.1293E-01$	$v_{17} : -5.1271E-01$	$v_{25} : -5.1272E-01$
$v_2 : -5.0722E-01$	$v_{10} : -5.0736E-01$	$v_{18} : -5.0746E-01$	$v_{26} : -5.0760E-01$
$v_3 : -4.6410E-01$	$v_{11} : -4.6437E-01$	$v_{19} : -4.6424E-01$	$v_{27} : -4.6451E-01$
$v_4 : -4.4188E-01$	$v_{12} : -4.4151E-01$	$v_{20} : -4.4165E-01$	$v_{28} : -4.4129E-01$
$v_5 : -4.4188E-01$	$v_{13} : -4.4165E-01$	$v_{21} : -4.4152E-01$	$v_{29} : -4.4129E-01$
$v_6 : -4.6410E-01$	$v_{14} : -4.6424E-01$	$v_{22} : -4.6431E-01$	$v_{30} : -4.6445E-01$
$v_7 : -5.0722E-01$	$v_{15} : -5.0746E-01$	$v_{23} : -5.0739E-01$	$v_{31} : -5.0764E-01$
$v_8 : -5.1292E-01$	$v_{16} : -5.1271E-01$	$v_{24} : -5.1294E-01$	$v_{32} : -5.1273E-01$

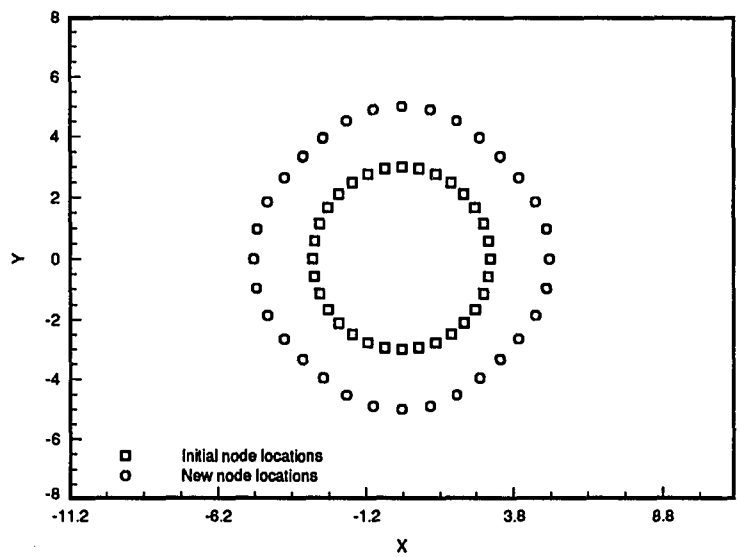

Figure 3.26: New opening shape for the square plate

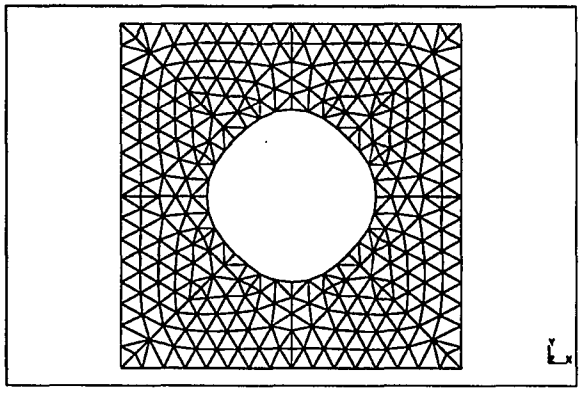

Figure 3.27: Finite element model of the modified plate (plate model)

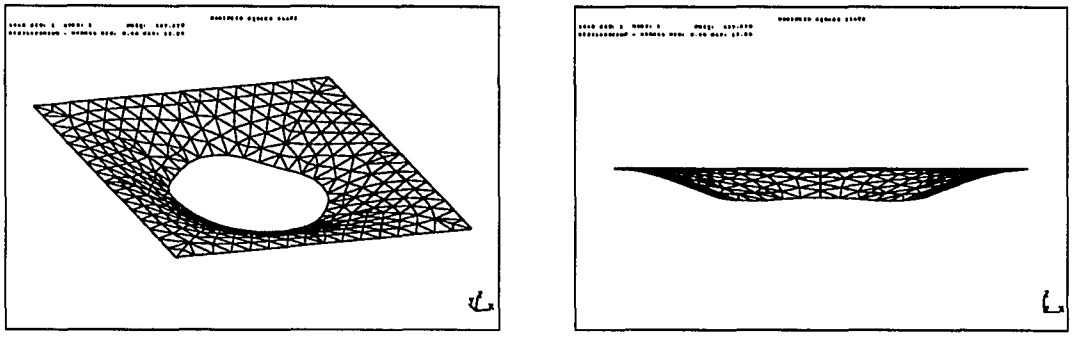

Figure 3.28: First mode of vibration, modified plate (plate model)

ing frequency of 197.4 Hz. This is a 38% increase from the calculated f_m of 143.4 Hz for the initial plate geometry of Figure 3.23.

In summary, the case studies given in this section showed that sensitivities for thin plates modeled with plate elements and NZS beam elements are essentially equivalent to corresponding sensitivities for thin plates modeled with solid elements and NZS plate elements. The resulting NZS beam sensitivities are used to modify the location of free edge nodes of plate structures in much the same way as they are used to modify the location of free surface nodes of solid structures.

4. APPLICATIONS: REDESIGN SUBJECT TO PARAMETER–BASED GEOMETRIC CONSTRAINTS

The pin geometry of Figure 4.1 will be used in this chapter as a case study for the parameter–based approach. The geometry and the loading are symmetric across the midplane of the pin; therefore, as shown by Figure 4.2, a half–pin finite element model is used in the analysis. Symmetric boundary conditions are applied to the midplane nodes. The surface nodes lying along the threaded portion are constrained in all degrees of freedom. This figure also shows NZS plate elements coating the free faces of the solid elements. As was the case for the cantilever beam of Chapter 3, the interior nodes are only coupled by solid elements; therefore, they have no rotational degrees of freedom. However, the surface nodes are shared by plate elements as well as solid elements. These nodes have rotational degrees of freedom in addition to their translational degrees of freedom.

4.1 Pin Under Point Loading

The first loading condition considered for the pin is a point load applied in the transverse direction at the top of the stem. Figures 4.3, 4.4, and 4.5 show contour plots of the maximum principal stress and the sensitivity of the stress in the solid element with the highest tensile stress, σ_h, with respect to the thickness of the plate

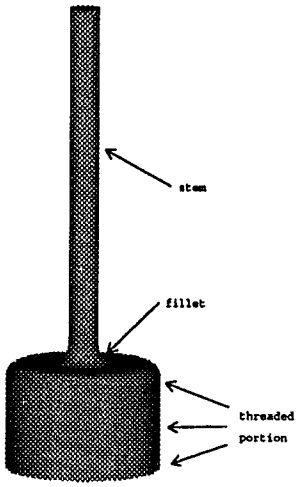

Figure 4.1: Pin geometry

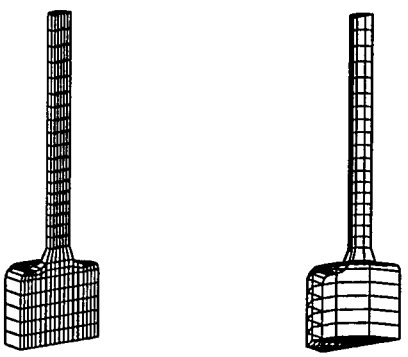

Figure 4.2: Pin finite element model and NZS plate elements

elements of Figure 4.2. The objective is to use these sensitivities to predict σ_h as the pin stem radius and/or fillet radius are changed.

Equation 2.11 of Chapter 2 takes on the form:

$$\sigma_h = \sigma_{h_o} + \sum_{k=1}^{N_k} \frac{\partial \sigma_h}{\partial v_k} V_k \tag{4.1}$$

with V_k representing the effective thickness for the kth NZS plate element computed using Equation 2.10.

Figure 4.6 shows the relocation of the surface nodes of the pin as the stem radius is reduced to 3.75 mm from its nominal value of 4.875 mm. For this change in the pin geometry, V_k assumes a negative value for the elements along the stem and the fillet and a value of zero elsewhere. This new design is designated as Design 2 in Table 4.1.

Table 4.1 shows that for Design 2, there is a 10.9% discrepancy between the σ_h predicted using Equation 4.1, and the corresponding value calculated by a FEA re–analysis. This table also presents calculations for two additional pin designs. In Design 3 the fillet radius is changed to 5.0 mm from its nominal value of 7.5 mm while the stem radius is set equal to that of Design 2. The discrepancy between predicted and calculated stress is 14.6% which is slightly higher than that of Design 2. In Design 4, however, the predicted stress of 108.6 kPa is much lower than the FEA result of 1323.0 kPa. We believe the explanation for this large discrepancy is that the model of Equation 4.1 is linear and therefore has a limited range of accuracy.

To investigate this matter, several more FEA runs were conducted with the fillet radius kept constant at the nominal value of 7.5 mm and the stem radius varying from 3 mm to 7 mm. Figure 4.7 presents results. As expected, the accuracy of the linear predictions diminishes for values of stem radius that are far from the neighborhood

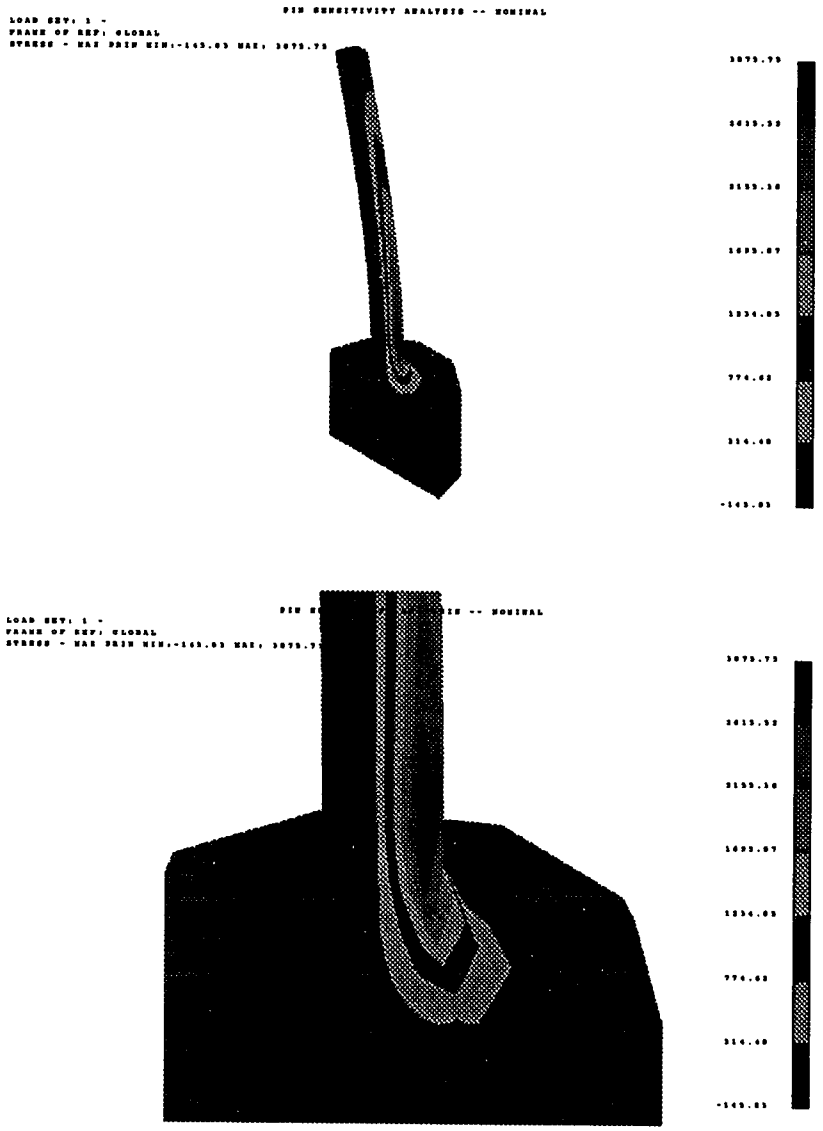

Figure 4.3: Maximum principal stress distribution (point loading)

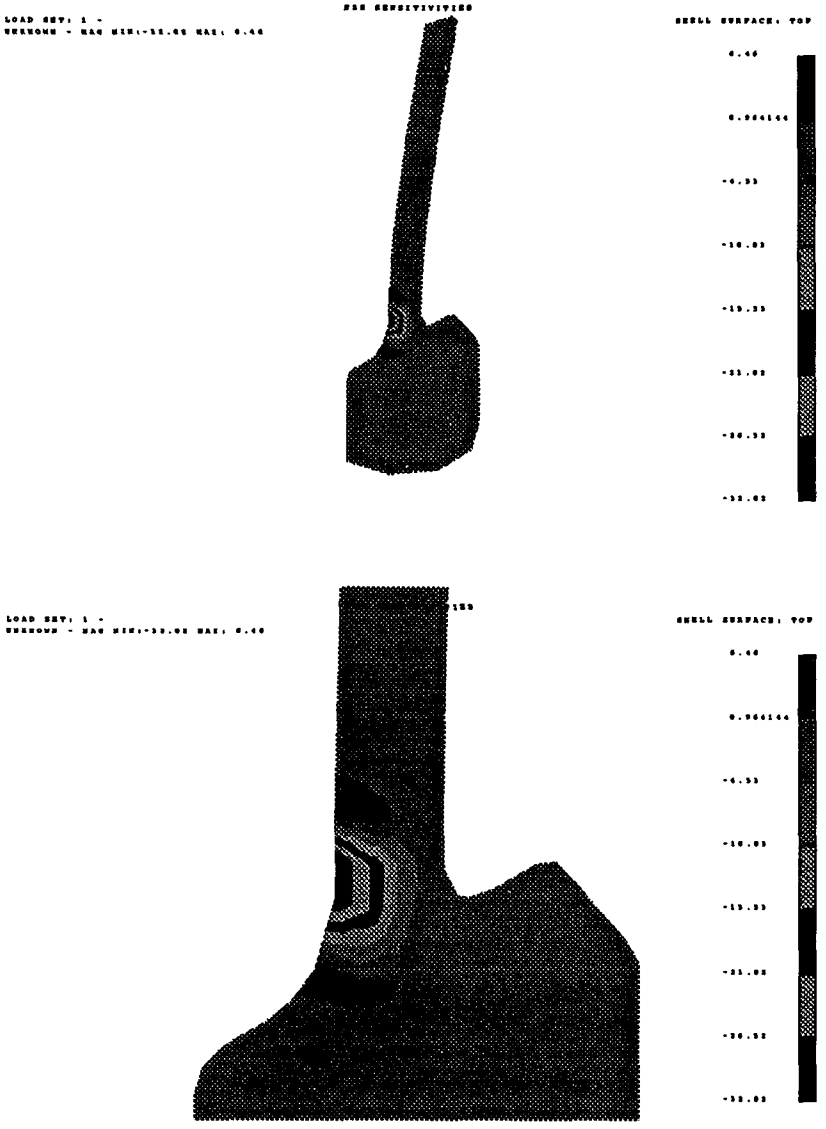

Figure 4.4: Sensitivity distribution, tension side (point loading)

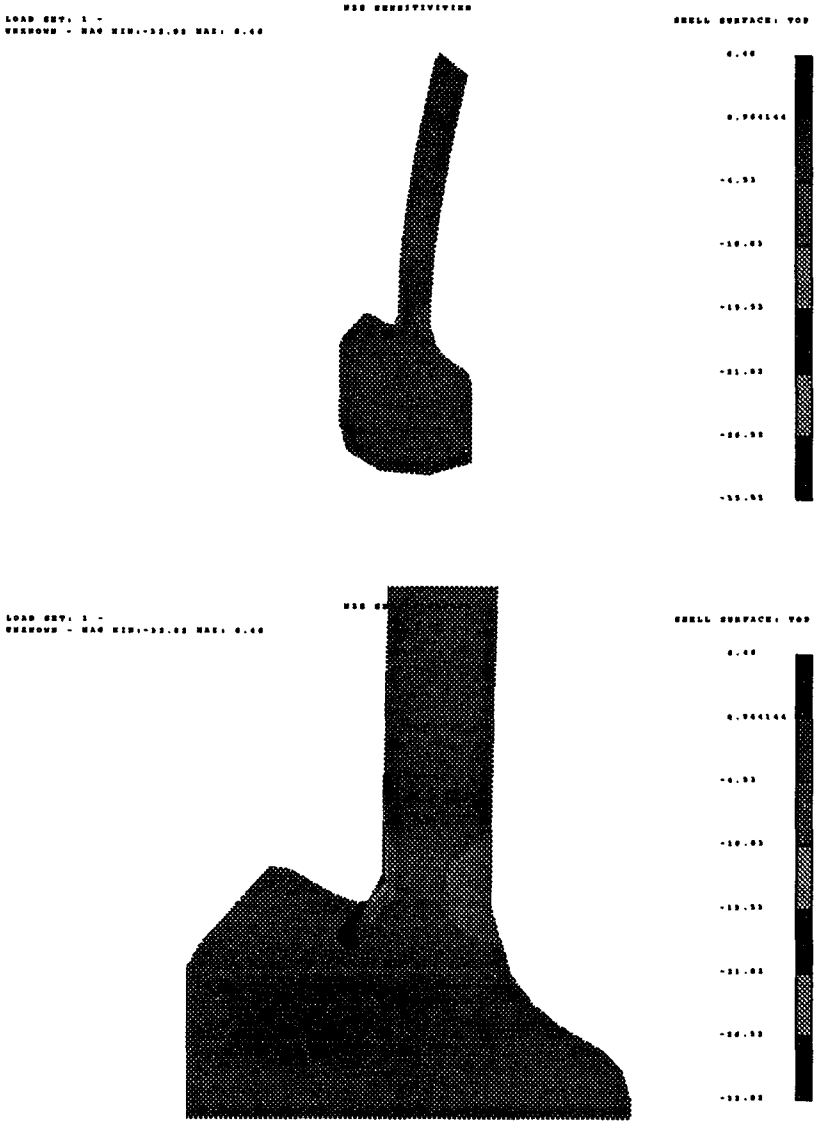

Figure 4.5: Sensitivity distribution, compression side (point loading)

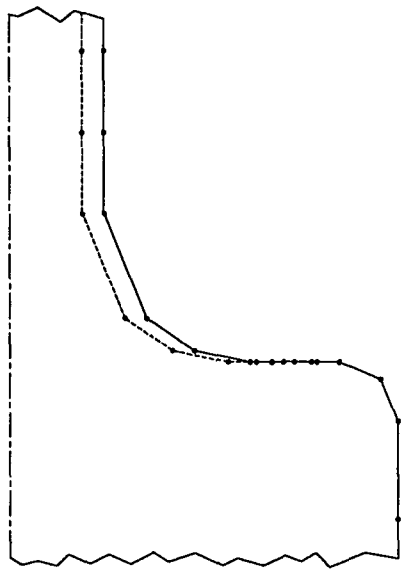

Figure 4.6: Relocation of the pin surface nodes (2D profile)

Table 4.1: Stress results for the pin geometry under point loading

Design number	Stem radius (mm)	Fillet radius (mm)	FEA σ_h (kPa)	Predicted σ_h (kPa)	Percent discrepancy
1 (nominal)	4.875	7.5	2372.7	—	—
2	3.75	7.5	5137.1	4574.3	10.9
3	3.75	5.0	5282.8	4511.7	14.6
4	6.0	5.0	1323.0	108.6	91.8

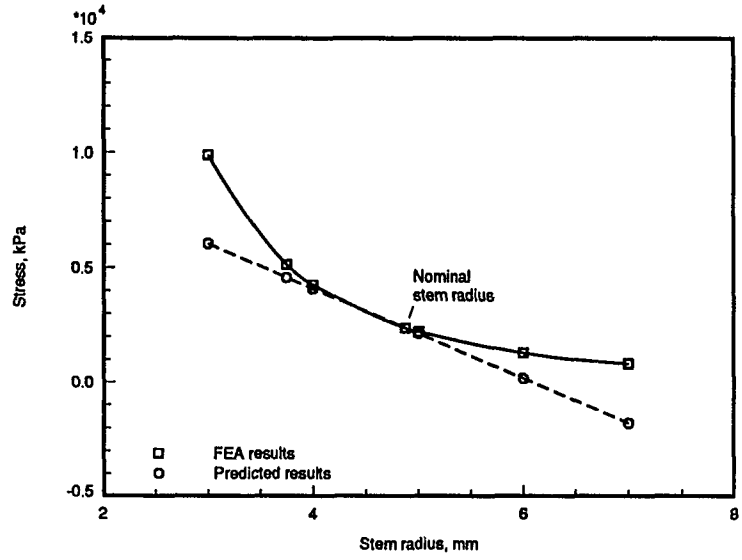

Figure 4.7: FEA results and sensitivity–based predictions (point loading)

of the nominal value.

It should be emphasized that the predictions of Table 4.1 were made based on the original FEA and the corresponding DSA. For this 2429 degrees of freedom structure, FEA and DSA took 3.0 and 2.9 minutes of CPU, respectively, on a DECstation 5000. Note also that the design changes are not limited to changes in a single dimensional parameter; i.e., the stem radius and the fillet radius can be changed simultaneously. Therefore, a linear model which allows prediction of stress with changes in the stem radius and/or fillet radius is built at a computational expense of 2.9 minutes, or roughly the expense of an additional FEA.

The predictions of Table 4.1 provide valuable insight on the behavior of the pin. In particular, the original FEA and the corresponding DSA indicate that σ_h has a significant dependence on the stem radius, but changes in the fillet radius are less important.

4.2 Pin Under Transverse Gravitational Loading

The loading is changed to a transverse gravitational loading to produce the stress distribution shown by Figure 4.8. Once again the objective is to predict the effect of changes in the value of the stress in the solid element with the highest tensile stress, σ_h, as the pin stem radius and/or fillet radius are changed.

Figure 4.9 shows the contour plot of $\frac{\partial \sigma_h}{\partial v_k}$ for the pin under gravitational loading. Comparison with Figures 4.4 and 4.5 suggests that in the fillet region, the sensitivities under gravitational loading are very similar to corresponding sensitivities under point loading.

However, the sensitivity distribution along the stem of the pin is quite different under gravitational loading. Figures 4.10 and 4.11 give the sensitivities along the upper 2/3 of the stem for both loading conditions. Under point loading the sensitivity is zero for all NZS elements which are far enough removed from the fillet region. For gravitational loading, the corresponding sensitivities are positive and assume their largest values at the free end of the pin. As in the case of the cantilever beam of Chapter 3, these sensitivities suggest that addition of material at the free end will increase the loading which in turn will have an unfavorable effect on the response.

The stem radius and fillet radius combinations of Table 4.1 are again used for the pin under gravitational loading. Table 4.2 presents the results. For ease of comparison of results, the magnitude of the gravitational loading is set such that σ_h for the nominal geometry is roughly equal to σ_h for the corresponding geometry under point loading.

As was the case with point loading, the predictions of Table 4.2 show that the stem radius has a larger influence on σ_h than the fillet radius. However, the level of

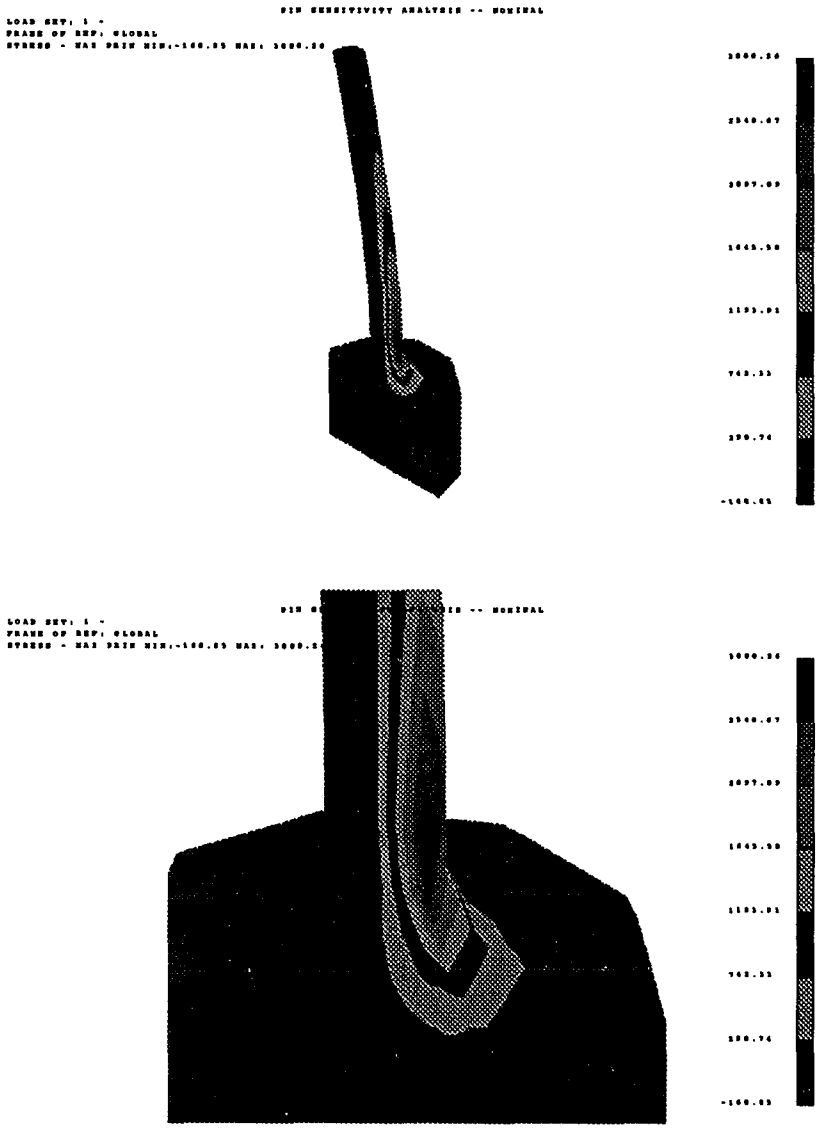

Figure 4.8: Maximum principal stress distribution (gravitational loading)

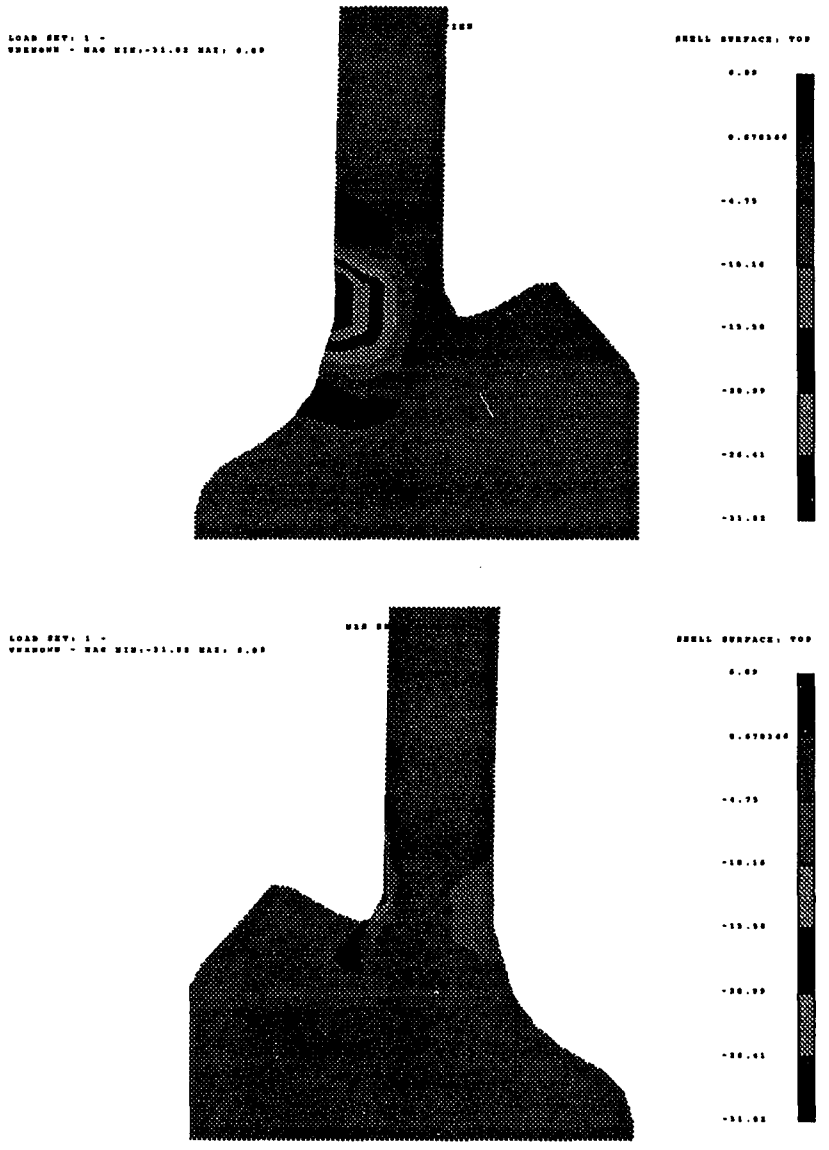

Figure 4.9: Sensitivity distribution (gravitational loading)

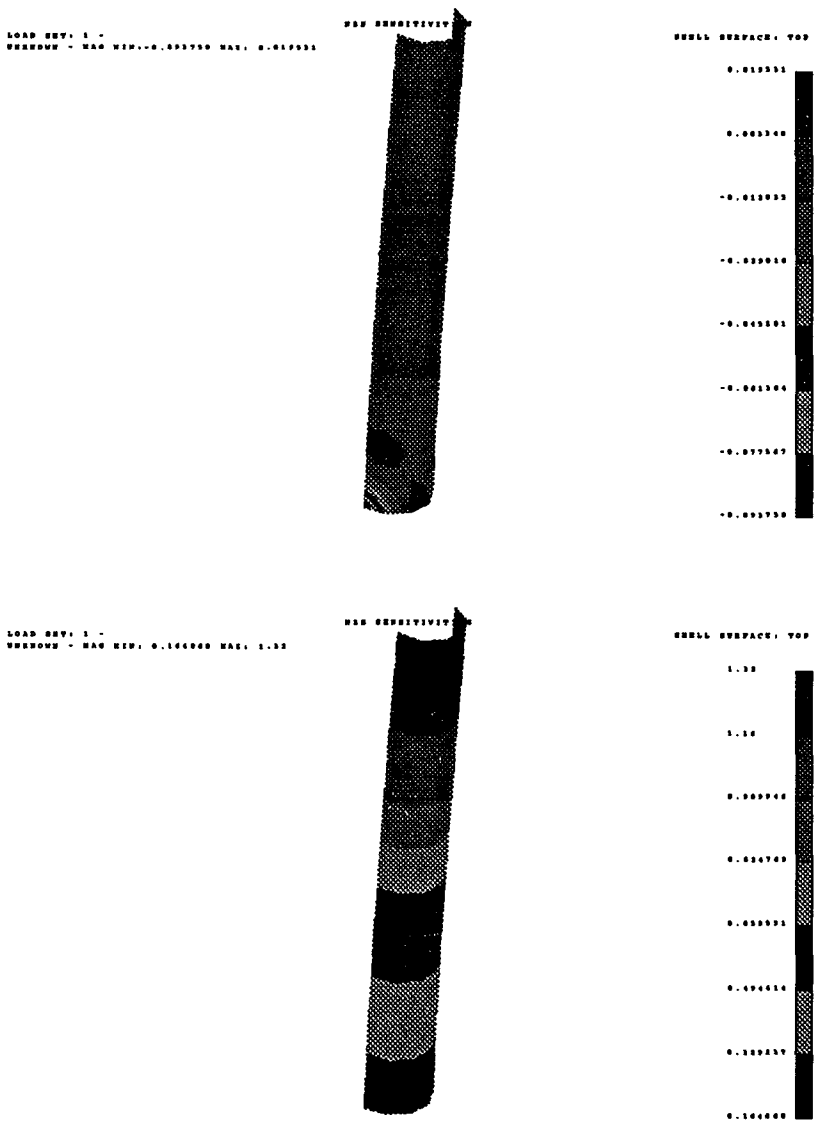

Figure 4.10: Sensitivity distribution along the upper 2/3 of the stem, tension side (point loading, top, and gravitational loading, bottom)

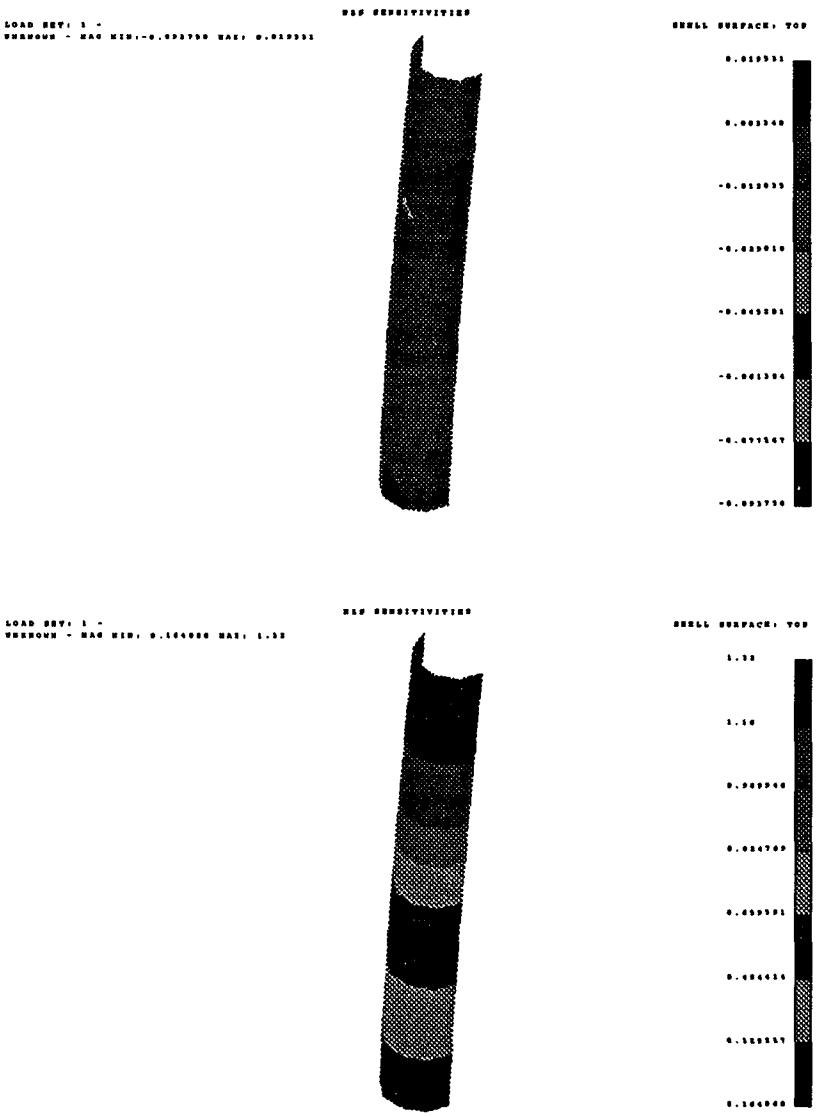

Figure 4.11: Sensitivity distribution along the upper 2/3 of the stem, compression side (point loading, top, and gravitational loading, bottom)

Table 4.2: Stress results for the pin geometry under gravitational loading

Design number	Stem radius (mm)	Fillet radius (mm)	FEA σ_h (kPa)	Predicted σ_h (kPa)	Percent discrepancy
1 (nominal)	4.875	7.5	2371.2	—	—
2	3.75	7.5	3056.1	3504.4	14.7
3	3.75	5.0	3233.8	3437.2	6.3
4	6.0	5.0	2053.9	1170.9	43.0

this influence is less severe under gravitational loading. For example, from Design 1 to Design 2, where the stem radius is reduced from 4.875 mm to 3.75 mm, the stress due to the point load is predicted to increase from its nominal value of 2372.7 kPa to a value of 4574.3 kPa, while the corresponding predicted increase under gravitational loading is from 2371.2 kPa to 3504.4 kPa. Using Equation 2.12, this leads to:

$$\left.\frac{\partial \sigma_h}{\partial r_s}\right)_{point\ load} = -1957.0\ kPa/mm$$
$$\left.\frac{\partial \sigma_h}{\partial r_s}\right)_{grav.\ load} = -1007.3\ kPa/mm \qquad (4.2)$$

where r_s represents the stem radius. This trend is expected since under a gravitational loading decreasing the stem radius has a dual effect of reducing the load as well as reducing the load carrying capacity, while under a point loading such a change only reduces the load carrying capacity.

Once again the results of Design 4 in Table 4.2 suggest that the linear model has a limited range of accuracy. Figure 4.12 presents the result of FEA runs corresponding to those given by Figure 4.7. Compared to the response under point loading, the stress versus stem radius relation exhibits a much more linear behavior under gravitational

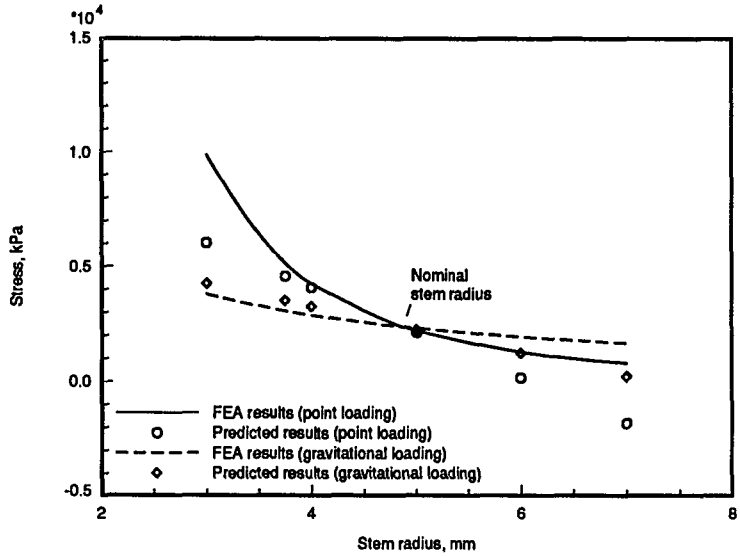

Figure 4.12: FEA results and sensitivity–based predictions (point loading and gravitational loading)

loading. This, in turn, translates to a wider range of accuracy for the linear model of Equation 4.1.

Under a gravitational load, the FEA and DSA for the nominal design required 3.2 and 5.9 minutes of CPU, respectively, on a DECstation 5000 (compared with 3.0 minutes for FEA and 2.9 minutes for DSA under a point loading).

In summary, application of the parameter–based approach to the pin structure leads to the conclusion that the maximum tensile stress is much more heavily dependent on the stem radius than the fillet radius. It also shows that the dependence is stronger under a point load than a gravitational load.

5. APPLICATIONS: REDESIGN SUBJECT TO PROPERTY–BASED GEOMETRIC CONSTRAINTS

In this chapter, we analyze the inverse elasticity problem of minimizing the stress concentration around an opening in a thin plate under biaxial loading. We will start with the plate shown in Figure 5.1 and use shape optimization to derive a better shape for the opening at the center of the plate.

The optimal solution to this problem is know to be a uniform tangential stress along the boundary of the opening (Ref. [7, 8, 9, 10, 11]). We will attack the problem by assuming that the maximum principal stress is in the tangential direction at the boundary of the opening, and attempting to change the shape of the opening to obtain a uniform maximum principal stress along the boundary.

Figure 5.1 presents the finite element model of the plate. The free edges of the plate elements surrounding the opening are lined with NZS beam elements which have the same length and depth dimensions as the edges of the underlying plate elements and a nearly zero thickness (see Figure 1.3).

For this example, the linear approximation of Equation 2.14 is formulated as:

$$\sigma_l = \sigma_{l_o} + \sum_{k=1}^{N_k} \frac{\partial \sigma_l}{\partial v_k} v_k \tag{5.1}$$

where σ_{l_o} is the original maximum principal stress in the lth high stress plate element, $\frac{\partial \sigma_l}{\partial v_k}$ is the sensitivity of the lth stress with respect to the kth NZS thickness, and v_k

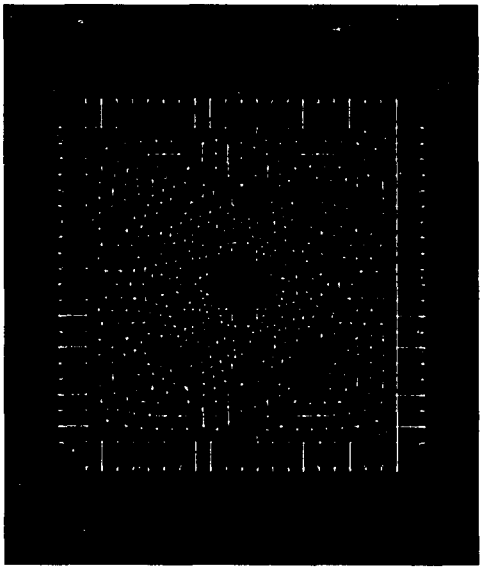

Figure 5.1: Finite element model of a 6" X 6" X 0.3" plate

is the kth thickness.

A desired stress level, $\overline{\sigma}_l$, for each high stress plate element is set by:

$$\overline{\sigma}_l = \sigma_{l_o} - \frac{1}{2}(\sigma_{l_o} - \overline{\sigma}) \tag{5.2}$$

where $\overline{\sigma}$ is some nominal stress (e.g., the nominal maximum principal stress away from the hole in the plate). The merit function of Equation 2.18, $f(R_l)$, is then expressed as:

$$f(R_l) = \sum_{l=1}^{N_l} \left(\frac{\sigma_l - \overline{\sigma}_l}{0.8(\sigma_{l_o} - \overline{\sigma}_l)} \right)^2 \tag{5.3}$$

A geometric constraint of keeping the hole area constant will be enforced:

$$g(\underline{\Delta}_i) = A_h - A_{h_o} = 0 \tag{5.4}$$

where A_{h_o} represents the hole area for the original plate geometry.

This constrained minimization problem (Equation 2.18) can be transformed to an unconstrained minimization problem:

$$min.\ F(R_l, \underline{\Delta}_i) \tag{5.5}$$

with $F(R_l, \underline{\Delta}_i)$ given by the function:

$$F = \left(\frac{A_h - A_{h_o}}{0.1A_{h_o}}\right)^2 + \sum_{l=1}^{N_l}\left(\frac{\sigma_l - \overline{\sigma}_l}{0.8(\sigma_{l_o} - \overline{\sigma}_l)}\right)^2 \tag{5.6}$$

The necessary condition for F to be minimized is:

$$\frac{\partial F}{\partial v_k} = 2\left(\frac{A_h - A_{h_o}}{0.1A_{h_o}}\right)\left(\frac{1}{0.1A_{h_o}}\right)\frac{\partial A_h}{\partial v_k}$$
$$+2\sum_{l=1}^{N_l}\left(\frac{\sigma_l - \overline{\sigma}_l}{0.8(\sigma_{l_o} - \overline{\sigma}_l)}\right)\left(\frac{1}{0.8(\sigma_{l_o} - \overline{\sigma}_l)}\right)\frac{\partial \sigma_l}{\partial v_k} = 0 \tag{5.7}$$

In general $\frac{\partial \sigma_l}{\partial v_k}$ and $\frac{\partial A_h}{\partial v_k}$ are nonzero; therefore, F is minimized when $\sigma_l = \overline{\sigma}_l$ (for all l high stress plate elements), and $A_h = A_{h_o}$.

As discussed in Chapter 2, the nodes surrounding the hole are moved based on the grid movement vector, $\underline{\Delta}_i$:

$$\underline{\Delta}_i = f(geom)d_r\frac{1}{v_{max}}\sum_{j=1}^{2} v_j\underline{\hat{n}}_j \tag{5.8}$$

where $f(geom)$ is a closed form, algebraic, geometry dependent function which yields a positive value; v_j is the thickness of the jth beam element surrounding node i; v_{max} is the maximum thickness magnitude (i.e., $max(|v_1|, |v_2|, |v_3|, \ldots, |v_{N_k}|)$); $\underline{\hat{n}}_j$ is the unit vector normal to the jth beam element with a positive direction pointing toward the interior of the hole; and d_r is a representative distance given by:

$$d_r = \frac{1}{N_k}\sum_{k=1}^{N_k}|v_k| \tag{5.9}$$

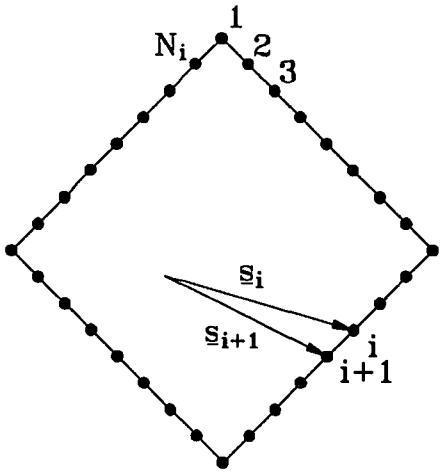

Figure 5.2: Calculation of the hole area

With arbitrary locations for the nodes surrounding the hole, the area of the opening, A_h, can be computed by:

$$A_h = \frac{1}{2}\left(\left|\underline{s}_1 \times \underline{s}_{N_i}\right| + \sum_{i=1}^{N_i-1} \left|\underline{s}_i \times \underline{s}_{i+1}\right|\right) \tag{5.10}$$

where $\underline{s}_i$ is a vector originating from a point in the plane of the hole and terminating at node i (see Figure 5.2).

In summary, given a trial thickness vector, v_k, stresses are predicted based on a linear model (Equation 5.1). The new locations of the nodes surrounding the hole are found using Equation 5.8, and the resulting hole area is calculated by Equation 5.10. An unconstrained minimization algorithm is used to find the design vector, v_k^*, which minimizes Equation 5.6.

5.1 Plate Under Even Biaxial Loading

Figure 5.1 shows the finite element model of a 6" X 6" X 0.3" steel plate with a 1 lb tensile force applied at each node along its four sides. The contour plot of

Figure 5.3: Maximum principal stress in the original plate, even biaxial loading

Figure 5.3 shows the resulting maximum principal stress field in the plate. As the plot shows, stress concentrations occur at the corners of the hole. The goal is to change the shape of this hole in order to minimize the stress concentration.

The high stress plate elements and the NZS beam elements are shown by Figure 5.4. These beam elements share the nodes along the free edges of the plate elements surrounding the hole, and are modeled as CBAR elements [16] with a 0.3" X 0.01" cross section (see Figure 1.3).

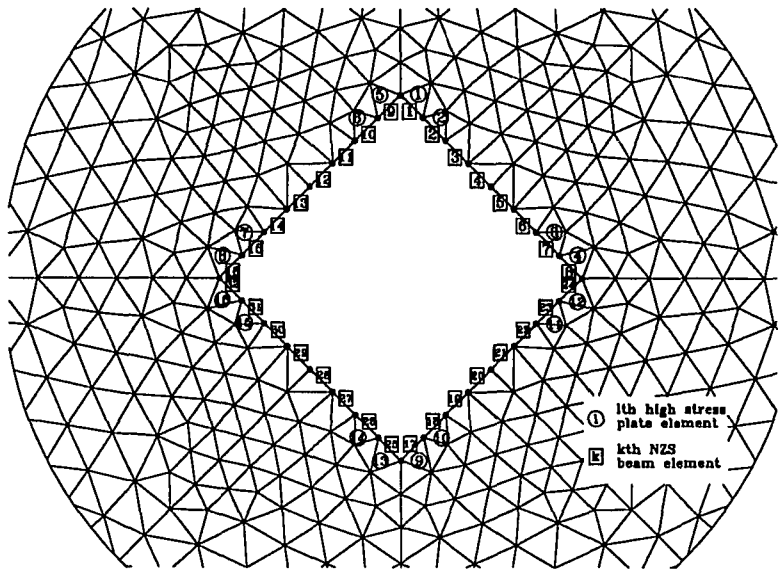

Figure 5.4: High stress plate elements and NZS beam elements

Tables 5.1 and 5.2 give the FEA and DSA results for the values of the maximum principal stresses in the high stress plate elements and the sensitivities of these stresses with respect to the nearly zero thickness dimension of the beam elements, respectively. As Figure 5.3 shows, the stress field is symmetric about the diagonal axes of the plate. This symmetry also holds for the sensitivities, for example, $\frac{\partial \sigma_4}{\partial v_8} = \frac{\partial \sigma_1}{\partial v_1}$, $\frac{\partial \sigma_4}{\partial v_6} = \frac{\partial \sigma_1}{\partial v_3}$, $\frac{\partial \sigma_{10}}{\partial v_{11}} = \frac{\partial \sigma_2}{\partial v_{27}}$. For the sake of space, Table 5.2 only gives the sensitivities of σ_1 and σ_2.

With the σ_{l_o} values of Table 5.1 and the $\frac{\partial \sigma_l}{\partial v_k}$ values of Table 5.2, the linear model of Equation 5.1 can be used to predict the stress levels for an arbitrary v_k. A $\overline{\sigma}$ of 12.5 psi is used in Equation 5.2. This is the nominal maximum principal stress away from the region of the hole.

For the hole geometry of Figure 5.4, $\underline{\hat{n}}_j$ in Equation 5.8 is the same for all beam elements on a given side of the hole (for example, $\underline{\hat{n}}_j = -0.707\underline{\hat{i}} - 0.707\underline{\hat{j}}$ for the

Table 5.1: Stress in the original plate, even biaxial loading

Stress variable	Stress value (psi)	Stress variable	Stress value (psi)
σ_1	3.6164E+01	σ_5	3.6164E+01
σ_2	1.7840E+01	σ_6	1.7840E+01
σ_3	1.7840E+01	σ_7	1.7840E+01
σ_4	3.6164E+01	σ_8	3.6164E+01

Table 5.2: NZS sensitivities, even biaxial loading ($\frac{\partial \sigma_l}{\partial v_k}$, psi/in)

σ_1	σ_2	σ_1	σ_2
$v_1 : -0.2015E+03$	$v_1 : 0.7948E+02$	$v_9 : 0.2896E+02$	$v_9 : 0.5811E+01$
$v_2 : 0.2827E+02$	$v_2 : -0.1771E+03$	$v_{10} : 0.9692E+01$	$v_{10} : 0.1025E+01$
$v_3 : 0.8984E+01$	$v_3 : 0.2526E+02$	$v_{11} : 0.3223E+01$	$v_{11} : 0.2075E+00$
$v_4 : 0.5078E+01$	$v_4 : 0.1105E+02$	$v_{12} : 0.2026E+01$	$v_{12} : 0.1709E+00$
$v_5 : 0.3467E+01$	$v_5 : 0.6482E+01$	$v_{13} : 0.1489E+01$	$v_{13} : 0.1343E+00$
$v_6 : 0.2881E+01$	$v_6 : 0.4443E+01$	$v_{14} : 0.1416E+01$	$v_{14} : 0.1709E+00$
$v_7 : 0.3320E+01$	$v_7 : 0.4443E+01$	$v_{15} : 0.1758E+01$	$v_{15} : 0.2319E+00$
$v_8 : 0.4858E+01$	$v_8 : 0.5566E+01$	$v_{16} : 0.2710E+01$	$v_{16} : 0.2808E+00$
$v_{17} : -0.2661E+01$	$v_{17} : -0.1221E+01$	$v_{25} : -0.2734E+01$	$v_{25} : -0.1660E+01$
$v_{18} : -0.1099E+01$	$v_{18} : -0.4639E+00$	$v_{26} : -0.1172E+01$	$v_{26} : -0.7813E+00$
$v_{19} : -0.5371E+00$	$v_{19} : -0.2075E+00$	$v_{27} : -0.6348E+00$	$v_{27} : -0.4639E+00$
$v_{20} : -0.3662E+00$	$v_{20} : -0.1343E+00$	$v_{28} : -0.5371E+00$	$v_{28} : -0.3784E+00$
$v_{21} : -0.2930E+00$	$v_{21} : -0.7324E-01$	$v_{29} : -0.4395E+00$	$v_{29} : -0.3662E+00$
$v_{22} : -0.2197E+00$	$v_{22} : -0.3662E-01$	$v_{30} : -0.4883E+00$	$v_{30} : -0.4028E+00$
$v_{23} : -0.9766E-01$	$v_{23} : 0.9766E-01$	$v_{31} : -0.5615E+00$	$v_{31} : -0.5737E+00$
$v_{24} : 0.6592E+00$	$v_{24} : 0.9277E+00$	$v_{32} : -0.5371E+00$	$v_{32} : -0.9399E+00$

Table 5.3: Solution for the first minimization problem, even biaxial loading

Thickness variable	Thickness value (in)	Thickness variable	Thickness value (in)
v_1^*	7.795E-02	v_5^*	-4.556E-02
v_2^*	4.330E-02	v_6^*	-5.739E-02
v_3^*	-5.739E-02	v_7^*	4.330E-02
v_4^*	-4.556E-02	v_8^*	7.795E-02

$k = 1, \ldots, 8$ edge in Figure 5.4). This is true for this initial minimization problem, but not so for subsequent problems since the sides of the hole will develop curvature as the hole shape is modified.

Minimization of Equation 5.6 yields the solution given by Table 5.3 for the $k = 1, \ldots, 8$ edge of the hole. As the table shows, the results are symmetric across the diagonal axes of the plate. Results for the other three edges correspond to those given in Table 5.3.

With the normal vectors in Equation 5.8 defined to be positive toward the interior of the hole, a positive v_k^* leads to the addition of material, and a negative v_k^* contributes to the removal of material. Table 5.3 shows that

$$v_k^* > 0 \qquad k = 1, 2, 7, 8 \tag{5.11}$$

$$v_k^* < 0 \qquad k = 3, 4, 5, 6 \tag{5.12}$$

This implies closure of the hole at the corners, and the expansion of the hole elsewhere. Figure 5.5 shows the location of the nodes surrounding the hole after the solution of the first optimization problem.

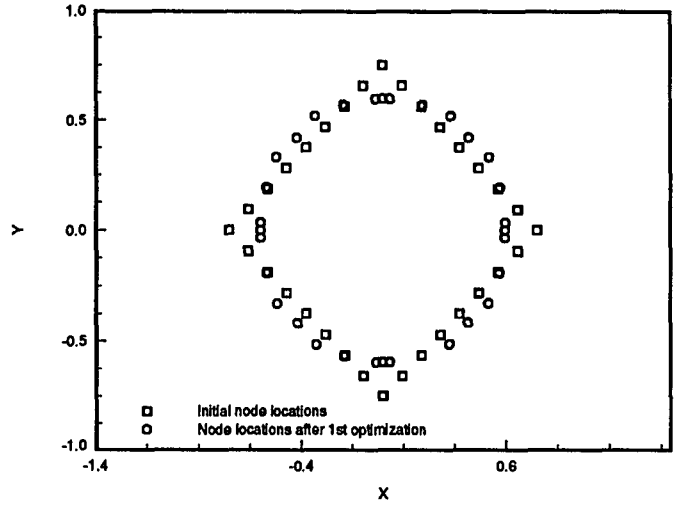

Figure 5.5: Modification of the hole shape, even biaxial loading

After a remeshing of the plate to conform to the new hole shape, a second FEA is conducted. Table 5.4 gives the maximum principal stresses along the $k = 1, \ldots, 8$ edge of the hole. For example, σ_5 represents the stress in the plate element which shares two nodes with beam element 5 in Figure 5.4. Once again, symmetry applies across the diagonals of the plate.

Comparison of Table 5.4 against Table 5.1 shows that the peak maximum principal stress is reduced from 36.2 psi to 25.8 psi. The maximum principal stress is also much more uniform along the boundary of the modified hole.

In the first optimization problem, $\overline{\sigma}$ in Equation 5.2 was set equal to 12.5 psi, the nominal maximum principal stress away from the hole. A uniform tangential stress along the boundary of the opening is known to be the optimality condition. The results of Table 5.4 show that the maximum principal stress (which is shortly verified to be in the tangential direction) is very close to being uniform. Therefore,

Table 5.4: Stress in the modified plate, even biaxial loading

Stress variable	Stress value (psi)	Stress variable	Stress value (psi)
σ_1	2.2413E+01	σ_5	2.3079E+01
σ_2	2.3937E+01	σ_6	2.5783E+01
σ_3	2.5783E+01	σ_7	2.3937E+01
σ_4	2.3079E+01	σ_8	2.2413E+01

in the ensuing optimization problem, $\overline{\sigma}$ is set equal to 23.8 psi, the average maximum principal stress in the plate elements surrounding the hole. There are 16 stress constraints which exceed this average: σ_2, σ_3, σ_6, and σ_7 for the $k = 1, \ldots, 8$ edge, and the corresponding stresses on the other edges.

With the FEA results of Table 5.4 and results of a second DSA, the linear model of Equation 5.1 is once again constructed. Minimization of Equation 5.6 and the application of Equation 5.8 to the solution yield the node locations shown by Figure 5.6. The figure indicates that the node locations do not vary appreciably, indicating convergence to the optimal hole shape.

A third FEA is conducted to find the stress distribution for the re-modified plate. The maximum principal stress is shown by the contour plot of Figure 5.7, and listed in Table 5.5 for the plate elements along the $k = 1, \ldots, 8$ edge of the hole. Comparison against Table 5.4 shows a reduction in the peak maximum principal stress from 25.8 psi to 24.7 psi.

Finally, Figure 5.8 shows the direction of the maximum principal stresses for

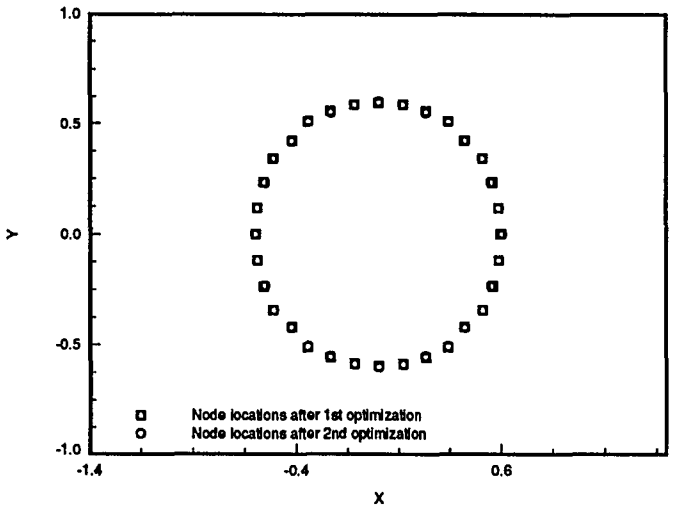

Figure 5.6: Re-modification of the hole shape, even biaxial loading

Table 5.5: Stress in the re-modified plate, even biaxial loading

Stress variable	Stress value (psi)	Stress variable	Stress value (psi)
σ_1	2.3555E+01	σ_5	2.3851E+01
σ_2	2.3363E+01	σ_6	2.4717E+01
σ_3	2.4717E+01	σ_7	2.3363E+01
σ_4	2.3851E+01	σ_8	2.3555E+01

Figure 5.7: Maximum principal stress in the re–modified plate, even biaxial loading

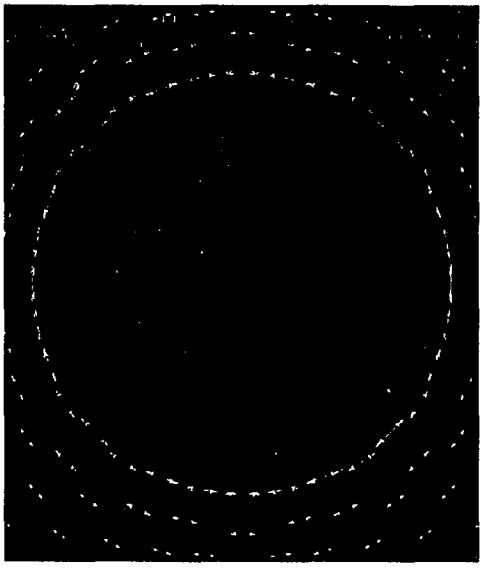

Figure 5.8: Maximum principal stress in the re–modified plate, even biaxial loading (arrow plot)

the re–modified plate. Clearly, the maximum principal stress is the tangential stress component along the hole boundary. Results of Table 5.5 show that the optimality condition of a uniform tangential stress along the hole boundary is essentially met.

In summary, after 3 FEA's and 2 size–based DSA's, the stress concentration factor was reduced from 2.89 to 1.98.

5.2 Plate Under Uneven Biaxial Loading

The forces applied to the plate of Figure 5.1 are now changed in order to create an uneven biaxial loading condition. In particular, a 1 lb tensile force is applied to each node along the left and right sides of the plate, and a 0.5 lb force is applied to the nodes along the top and bottom sides. Figure 5.9 and Table 5.6 give the resulting maximum principal stress field and the corresponding stress values for the

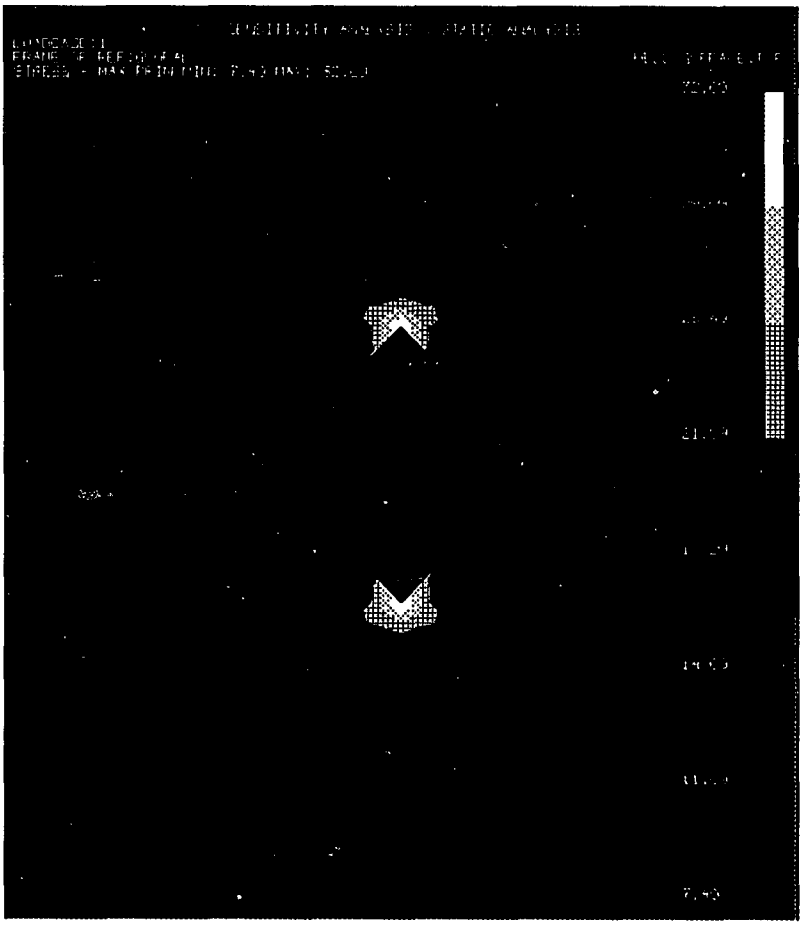

Figure 5.9: Maximum principal stress in the original plate, uneven biaxial loading

plate elements along the $k = 1,\ldots,8$ edge of Figure 5.4. Under uneven biaxial loading, symmetry holds across the vertical and horizontal axes of symmetry of the plate.

The nominal maximum principal stress away from the hole remains unchanged at 12.5 psi. Setting $\overline{\sigma}$ equal to 12.5 psi, σ_1, σ_2, σ_8 and the corresponding stress variables on the other three edges of the hole become the active stress constraints. Table 5.7 presents the sensitivities of these stress variables with respect to the nearly zero

Table 5.6: Stress in the original plate, uneven biaxial loading

Stress variable	Stress value (psi)	Stress variable	Stress value (psi)
σ_1	4.1197E+01	σ_5	7.4740E+00
σ_2	1.9627E+01	σ_6	6.8026E+00
σ_3	1.1753E+01	σ_7	7.2633E+00
σ_4	9.4142E+00	σ_8	1.3061E+01

thickness dimension of the beam elements of Figure 5.4.

Table 5.8 and Figure 5.10 give the solution for the first minimization problem and the corresponding new locations for the nodes surrounding the hole, respectively. Subsequent remeshing and FEA gives the results shown in the second column of Table 5.9. The peak maximum principal stress has reduced from 41.2 psi to 36.1 psi.

Table 5.9 shows that the maximum principal stress around the hole is still quite nonuniform after the first iteration. Therefore, the overall shape optimization problem continues.

Table 5.9 shows four more iterations of the optimization problem. Each iteration entails a FEA and DSA, as well as remeshing for iterations which result in large changes in the hole geometry. As noted in the table, $\overline{\sigma}$ is set equal to the nominal maximum principal stress away from the hole for the first two iterations, while it is set to the average maximum principal stress in the plate elements surrounding the hole for subsequent iterations. Figure 5.11 shows the node locations corresponding to the iterations of Table 5.9.

Table 5.7: NZS sensitivities, uneven biaxial loading ($\frac{\partial \sigma_i}{\partial v_k}$, psi/in)

σ_1	σ_2	σ_8
$v_1 : -0.2251E+03$	$v_1 : 0.9020E+02$	$v_1 : 0.5566E+01$
$v_2 : 0.2998E+02$	$v_2 : -0.1870E+03$	$v_2 : 0.3613E+01$
$v_3 : 0.8398E+01$	$v_3 : 0.2240E+02$	$v_3 : 0.2734E+01$
$v_4 : 0.4199E+01$	$v_4 : 0.8716E+01$	$v_4 : 0.2905E+01$
$v_5 : 0.2393E+01$	$v_5 : 0.4199E+01$	$v_5 : 0.3516E+01$
$v_6 : 0.1660E+01$	$v_6 : 0.2429E+01$	$v_6 : 0.5200E+01$
$v_7 : 0.1465E+01$	$v_7 : 0.1856E+01$	$v_7 : 0.1262E+02$
$v_8 : 0.1856E+01$	$v_8 : 0.2039E+01$	$v_8 : -0.7736E+02$
$v_9 : 0.3286E+02$	$v_9 : 0.6787E+01$	$v_9 : 0.8057E+00$
$v_{10} : 0.1055E+02$	$v_{10} : 0.1209E+01$	$v_{10} : -0.8545E-01$
$v_{11} : 0.3076E+01$	$v_{11} : 0.2441E+00$	$v_{11} : -0.1831E+00$
$v_{12} : 0.1709E+01$	$v_{12} : 0.1709E+00$	$v_{12} : -0.1953E+00$
$v_{13} : 0.1025E+01$	$v_{13} : 0.1099E+00$	$v_{13} : -0.2197E+00$
$v_{14} : 0.7813E+00$	$v_{14} : 0.1099E+00$	$v_{14} : -0.2686E+00$
$v_{15} : 0.7813E+00$	$v_{15} : 0.1099E+00$	$v_{15} : -0.4273E+00$
$v_{16} : 0.1074E+01$	$v_{16} : 0.1099E+00$	$v_{16} : -0.9766E+00$
$v_{17} : -0.3027E+01$	$v_{17} : -0.1367E+01$	$v_{17} : 0.2979E+01$
$v_{18} : -0.1172E+01$	$v_{18} : -0.5005E+00$	$v_{18} : 0.1843E+01$
$v_{19} : -0.5371E+00$	$v_{19} : -0.2075E+00$	$v_{19} : 0.1294E+01$
$v_{20} : -0.3418E+00$	$v_{20} : -0.1343E+00$	$v_{20} : 0.1209E+01$
$v_{21} : -0.2441E+00$	$v_{21} : -0.7324E-01$	$v_{21} : 0.1331E+01$
$v_{22} : -0.1465E+00$	$v_{22} : -0.3662E-01$	$v_{22} : 0.1733E+01$
$v_{23} : -0.4883E-01$	$v_{23} : 0.2441E-01$	$v_{23} : 0.4004E+01$
$v_{24} : 0.2441E+00$	$v_{24} : 0.3296E+00$	$v_{24} : 0.1056E+02$
$v_{25} : -0.3076E+01$	$v_{25} : -0.1843E+01$	$v_{25} : -0.6348E+00$
$v_{26} : -0.1221E+01$	$v_{26} : -0.8179E+00$	$v_{26} : -0.6592E+00$
$v_{27} : -0.5371E+00$	$v_{27} : -0.4150E+00$	$v_{27} : -0.4883E+00$
$v_{28} : -0.3906E+00$	$v_{28} : -0.3052E+00$	$v_{28} : -0.4150E+00$
$v_{29} : -0.2930E+00$	$v_{29} : -0.2319E+00$	$v_{29} : -0.3662E+00$
$v_{30} : -0.2441E+00$	$v_{30} : -0.2075E+00$	$v_{30} : -0.3784E+00$
$v_{31} : -0.1953E+00$	$v_{31} : -0.2319E+00$	$v_{31} : -0.5249E+00$
$v_{32} : -0.1465E+00$	$v_{32} : -0.3174E+00$	$v_{32} : -0.1025E+01$

Table 5.8: Solution for the first minimization problem, uneven biaxial loading

Thickness variable	Thickness value (in)	Thickness variable	Thickness value (in)
v_1^*	8.801E-02	v_5^*	-1.739E-02
v_2^*	6.042E-02	v_6^*	-1.723E-02
v_3^*	-3.338E-02	v_7^*	-2.379E-02
v_4^*	-2.097E-02	v_8^*	1.174E-02

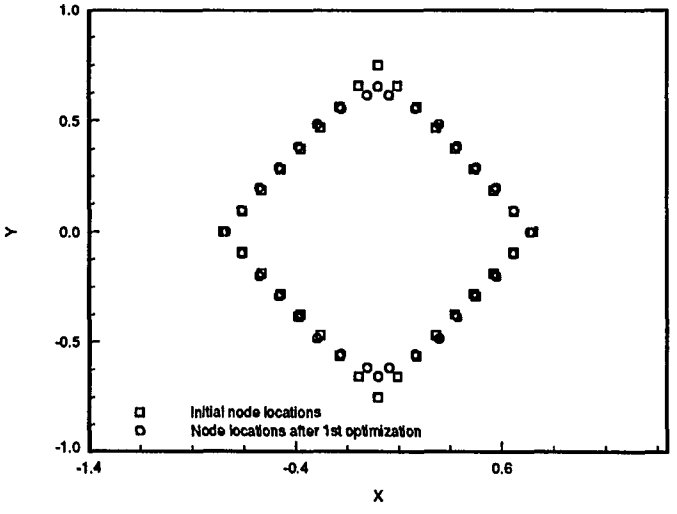

Figure 5.10: Modification of the hole shape, uneven biaxial loading

Table 5.9: Results of hole shape modifications, uneven biaxial loading (psi)

	Original plate	Iteration 1	Iteration 2	Iteration 3	Iteration 4	Iteration 5
σ_1	41.197	36.083	27.312	24.436	21.939	20.318
σ_2	19.627	22.604	18.013	19.694	19.558	18.630
σ_3	11.753	19.113	14.865	18.629	20.064	19.280
σ_4	9.4142	13.849	16.778	19.341	19.996	18.398
σ_5	7.4740	9.7509	21.233	20.776	20.379	20.780
σ_6	6.8026	8.8304	18.714	17.955	18.291	20.962
σ_7	7.2633	9.2379	13.464	13.981	14.064	14.961
σ_8	13.061	14.094	12.922	13.782	13.685	13.325
$\overline{\sigma}$	12.5	12.5	17.9	18.6	18.5	—
Active stress constraint	σ_1,σ_2 σ_8	σ_1,σ_2 σ_3,σ_4 σ_8	σ_1,σ_2 σ_5,σ_6	σ_1,σ_2 σ_4,σ_5	σ_1,σ_2 σ_3,σ_4 σ_5	—

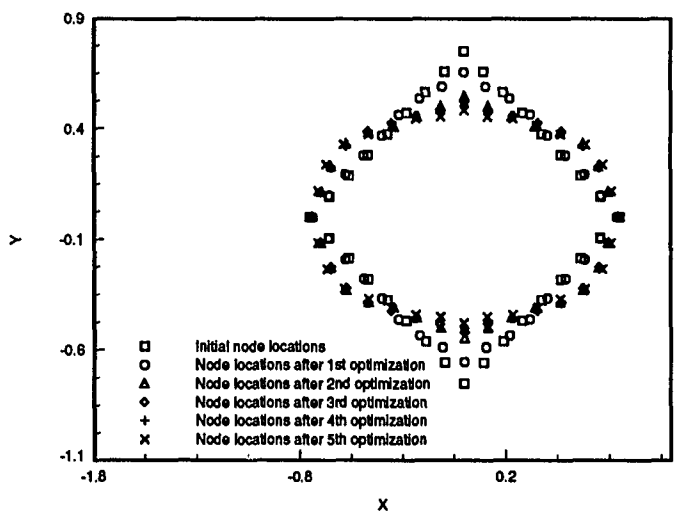

Figure 5.11: Re–modifications of the hole shape, uneven biaxial loading

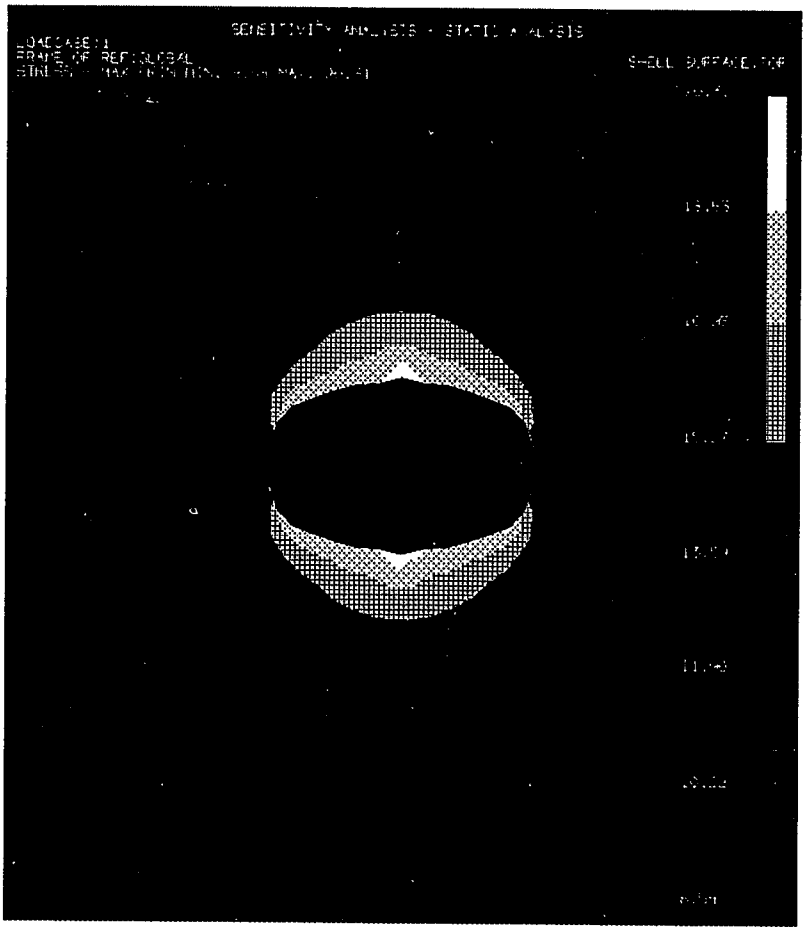

Figure 5.12: Maximum principal stress in the final plate geometry, uneven biaxial loading

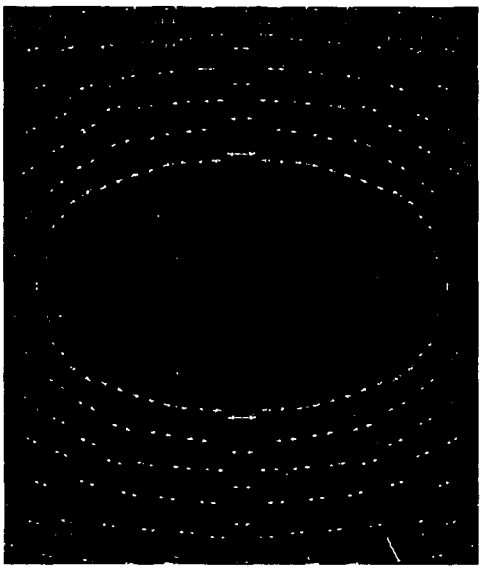

Figure 5.13: Maximum principal stress in the final plate geometry, uneven biaxial loading (arrow plot)

Figures 5.12 and 5.13 present the contour plot and arrow plot of the maximum principal stress for the final plate geometry, respectively. As was the case with even biaxial loading, the direction of the maximum principal stress is tangent to the hole boundary.

In summary, 6 FEA's and 5 size–based DSA's were used to reduce the stress concentration under uneven biaxial loading from 3.30 to 1.68 or by 48%. This compares to a 31% reduction for the plate under even loading.

6. CONCLUSIONS

This thesis presented a new method for finite–element–based shape redesign which uses size sensitivities to guide shape redesign. Since only relatively inexpensive size sensitivities are used in this method, the method has an advantage over shape redesign methods which require the calculation of expensive shape sensitivities.

The method is based on the introduction of a thin layer of elements, so–called NZS elements, on selected free surfaces of an existing finite element model of a structure. For structures modeled with solid elements, plate elements are used to coat the free faces of solid elements, while for structures modeled with plate elements, beam elements are used to line the free edges of plate elements. Since NZS elements are very thin, the incorporation of these elements does not significantly change the response of the structure. Sensitivities of the response with respect to the thickness of these elements provide qualitative insight on the behavior of the structure as well as a quantitative basis for shape optimization.

Application of the method to several small to medium–sized problems (up to 6220 degrees of freedom, and 569 size sensitivity calculations) involving displacement, stress, and natural frequency response variables, and geometric constraints showed that the method provides an effective and efficient means of shape redesign.

BIBLIOGRAPHY

[1] Botkin, M. E., Bennett, J. A. "Shape Optimization of Three–dimensional Folded Plate Structures." AIAA J. 23 (11) (1985): 1804–1810.

[2] Kikuchi, N., Chung, K. Y., Torigaki, T., Taylor, J. E. "Adaptive Finite Element Methods for Shape Optimization of Linear Elastic Structures." Presented at the General Motors Conference: The Optimal Shape, Warren, MI, May, 1985.

[3] Haftka, R. T., Grandhi, R. V. "Structural Shape Optimization–A Survey." Computer Methods in Applied Mechanics and Engineering 57 (1986): 97–98.

[4] Mikaili, A., Bernard, J. E. "Structural Redesign Using Nearly Zero Section Reinforcements." Journal of Finite Elements in Analysis and Design, Vol. 11 (1992): 221-233.

[5] I–DEAS Finite Element Modeling User's Guide, Version V, Structural Dynamics Research Corporation, Milford, OH, 1990: 24.11–24.21.

[6] MSC/NASTRAN User's Manual Volume II, Version 66A, The MacNeal–Schwendler Corporation, Los Angeles, CA, November 1988: 3.1–1.

[7] Cherpanov, G.P. "Inverse Problems of the Plane Theory of Elasticity." Prikl. Mat. Mekh. 38 (6) (1974): 963-979.

[8] Dhir, S.K. "Optimization in a Class of Hole Shapes in Plate Structures." ASME J. Appl. Mech. 48 (1981): 905-908.

[9] Dhir, S.K. "Optimization of Openings in Plates." AIAA/ASME/ASCE/AHS 23rd Structural Dynamics and Materials Conference, AIAA-82-0717, New Orleans, LA, 1982.

[10] Dhir, S.K. "Optimization of Openings in Plates Under Plane Stress." AIAA J. 21 (10) (1983): 1444-1447.

[11] Weck, M., Steinke, P. "An Efficient Technique in Shape Optimization." J. Structural Mech. 11 (4) (1983/84): 433-449.

[12] Vanderplaats, G. N., Numerical Optimization Techniques for Engineering Design: With Applications. McGraw-Hill, New York, 1984.

[13] Somayajula, G., Interactive Optimization of Mechanical Systems with Multiple Performance Requirements. Ph.D. Dissertation, Iowa State University, Ames, Iowa, 1989.

[14] Shigley, E. S., Mitchell, L. D. Mechanical Engineering Design. McGraw-Hill, New York, 1983.

[15] MSC/NASTRAN Application Manual Volume II, Version 66A, The MacNeal–Schwendler Corporation, Los Angeles, CA, April 1983: 3.4–28.

[16] MSC/NASTRAN User's Manual Volume I, Version 66A, The MacNeal-Schwendler Corporation, Los Angeles, CA, November 1988: 1.3-4.